博士論文

Verification and application of electron energization process during spherical tokamak merging start-up

（球状トカマク合体立ち上げにおける電子エネルギー付与過程の検証と応用）

指導教員：井 通暁 准教授

Academic Supervisor: Prof. M. Inomoto

東京大学大学院　新領域創成科学研究科

複雑理工学専攻

Department of Complexity Science and Engineering
Graduate School of Frontier Sciences
The University of Tokyo

牛木知彦

Tomohiko Ushiki

Abstract

Spherical tokamak (ST) merging start-up is one of the potential candidates of the CS-free start-up methods because of the rapid plasma heating through magnetic reconnection and resulting high beta characteristic. To achieve high-performance ST which can be connected to additional heating by RF or NBI using ST merging it is necessary for optimizing reconnection heating during merging. In this thesis the electron energization mechanism during ST merging start-up, which has not experimentally verified yet, was primarily investigated in University of Tokyo Spherical Tokamak (UTST) experiment.

In ST merging, which includes the reconnection event in the presence of the guide field, characteristic electron acceleration is predicted by numerical studies. The investigation has shown that the electrons near the X point or downstream region are effectively accelerated in toroidal direction by the parallel electric field during plasma merging. The spatial profile of the accelerated electrons depend on the time phase during merging. In early phase accelerated electrons spread relatively wide area at downstream region. Finally, in the almost steady phase of the reconnection the profile become the left-right asymmetric structures along a pair of the separatrix. These results will be important knowledges for optimizing reconnection heating during ST merging.

Furthermore, to investigate how the accelerated electrons affect the final ST equilibrium after merging, particularly the electron temperature, plasma shape reconstruction technique of merging plasma which is the necessary technique for evaluating the electron heating efficiency during merging start-up quantitatively was developed. The Modified Cauchy condition surface (M-CCS) method has been applied to reconstruct the plasma boundary shape as well as the eddy current profile for merging ST in the UTST and the ST40. In the test calculation based on the reference poloidal flux profile both of the UTST and the ST40 merging operation, the plasma boundary shape has been reconstructed accurately and the eddy current profile has been also reconstructed with fairly good accuracy. From these test calculations preparation for experimental verification in the UTST was completed.

Contents

List of figures

List of tables

Chapter 1

Introduction

1.1 Nuclear Fusion

Nuclear Fusion is a phenomena in which light nuclei approach and fuse together to form a heavier nucleus. Then huge energy is released due to the mass defect following the equation $E = mc^2$. This reaction occurs in the central region of the sun or star and the energy generated by the reaction is considered as energy source of them. The nuclear fusion reaction has also been studied toward the use for a power plant. With regard to artificial generation of nuclear fusion, the reaction between deuterium and tritium, so-called "DT fusion reaction", indicated in Equation (1.1) and Fig.1.1 with largest cross section is considered as the strong candidate.

$$D + T \rightarrow He^4\ (3.52MeV) + n\ (14.06MeV) \tag{1.1}$$

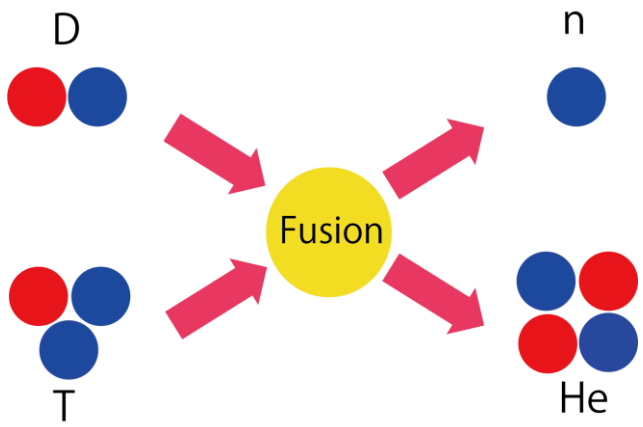

Fig.1.1 DT reaction

Fusion power plant is widely noticed as sustainable energy source because deuterium and lithium, which is the source of tritium, is abundant in ocean resource. To achieve burning condition of fusion reaction, hot plasma with temperature higher than a billion [K] should be confined in a reactor. So magnetic confinement of plasma have been widely studied. The mainstream of magnetic confinement concept is called 'Tokamak', using helically twisted magnetic field covering torus surface. This concept is employed in the international thermonuclear experimental reactor (ITER) which is being constructed in France.

1.2 Spherical Tokamak

Conceptual diagram of tokamak is shown in Fig.1.2 (a). R and a indicate plasma major radius and plasma minor radius. Aspect ratio A is defined as a ratio of plasma major radius to plasma minor radius. Spherical tokamak (ST) [1] is a variant of a tokamak with a small aspect ratio, generally less than 2 and has been studied to develop compact and economical fusion reactor. The beta value is an important value as the economic barometer of the fusion reactor. The volume average beta value is given by the ratio of plasma thermal pressure to magnetic pressure as

$$\langle \beta \rangle = \frac{\langle p \rangle}{\langle B^2 \rangle / 2\mu_0}, \tag{1.2}$$

where $\langle p \rangle$ is volume average plasma thermal pressure, B is magnetic field and μ_0 is vacuum permeability. Since this value is very close to the toroidal average beta in tokamak research, in tokamak research $\langle \beta \rangle$ is usually replaced by toroidal beta value $\beta_t = \langle p \rangle / \left(\langle B_t^2 \rangle / 2\mu_0 \right)$, where B_t is toroidal magnetic field. Then fusion output power P is given as

$$P \propto \beta_t B_t^4 V \tag{1.3}$$

where V is plasma volume. From eq.(1.3) increasing toroidal beta value is necessary to realize economic fusion reactor which provides larger electricity with smaller plant scale.

But the toroidal beta value is limited by plasma instability and its scaling in tokamak plasma was shown by Troyon as [1]

$$\beta_{t_{\max}} = \frac{\beta_N I_p}{aB_t} = \frac{5\kappa\beta_N}{q_j A}, \tag{1.4}$$

where β_N is the normalized beta value, I_p is the total plasma current, κ is the elongation of the plasma shape, q_j is the safety factor at the plasma edge. Eq.(1.4) implies that the higher beta value will be achieved in tokamak configuration with lower aspect ratio. So the ST has advantage of high beta capability.

Furthermore the high normalized beta capability is another remarkable advantage of the ST. The

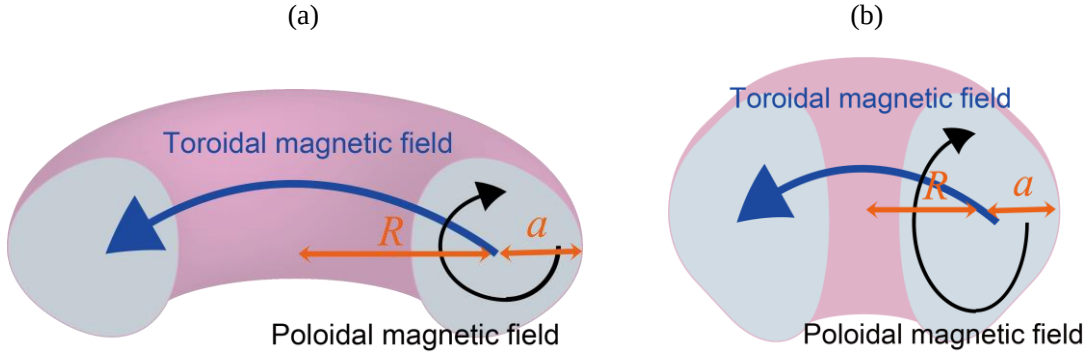

Fig.1.2 (a) Conceptual diagram of tokamak and (b) spherical tokamak

normalized beta has the relation between β_t and $\beta_p = \langle p \rangle / \left(\langle B_p^2 \rangle / 2\mu_0 \right)$, where B_p is poloidal magnetic field, as

$$\beta_t \beta_p = 25\left(\frac{1+\kappa^2}{2}\right)\left(\frac{\beta_N}{100}\right)^2 . \tag{1.5}$$

The poloidal beta is very important value for driving bootstrap current which is necessary for realizing steady operation of fusion reactors because fraction of bootstrap current is approximated as

$$f_{boot} = \frac{C_1}{A^{0.5}}\beta_p , \tag{1.6}$$

where $C_1 = 0.67$ is given by Cordey [2]. From Eq.(1.6), to increase the fraction of bootstrap current decreasing the aspect ratio or increasing poloidal beta is necessary. However Eq.(1.5) implies that β_t for the fusion power production and β_p for the high fraction of bootstrap current have trade-off relation. To increase both β_t and β_p simultaneously, it is important to increase κ or β_N. The scaling of $\beta_N \propto 12/A$ was also reported by R.D. Stambaugh et.al [3]. This dependence on the aspect ratio has been demonstrated in the ST experiments of the world. Figure 1.3 shows the experimentally achieved toroidal beta value for the ST and the conventional tokamak [4]. Figure. 1.3 shows that very high normalized beta up to about 6.5 was achieved in ST experiments even though the normalized beta limit of the conventional tokamak was about 3.5. From this high normalized beta capability, higher bootstrap current drive can be expected. In the tokamak experiments about 90 % bootstrap current already has been demonstrated [5]. However, in the ST almost 100 % bootstrap current is predicted [1, 6, 7]. Thus the ST has promising configuration which has capability of both high beta and steady operation.

Nevertheless, the start-up scenario of ST as a reactor has not yet been well established because it is not advantageous to employ conventional inductive current ramp-up schemes using a central solenoid (CS) coil. Because the small aspect ratio of an ST reduces the available space in the central region of a vacuum vessel, the CS coil significantly restricts the flexibility of the reactor design. Therefore, the development of a CS-free start-up method is

one of the most important issues facing ST reactors. Various types of start-up methods, such as introductions of the electron cyclotron wave, the electron Bernstein wave [8, 9], the lower hybrid wave [10], the coaxial helicity injection [11-14], the induction by vertical field coil [15-17], and the merging technique [18, 19], are being developed in many experimental devices.

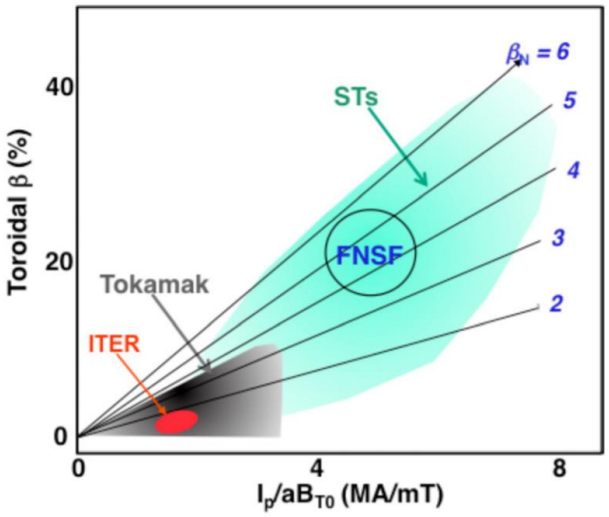

Fig.1.3 Experimentally achieved plasma beta values for STs and conventional tokamak [4].

1.3 Spherical tokamak merging start-up

The ST merging start-up method has been demonstrated in START, MAST (UKAEA) [20], TS-3, TS-4 (Univ. Tokyo) [18] and UTST [19]. This method has the advantage of achieving high plasma temperature, and beta value as well because it involves the reconnection heating and the compression processes. The direct ion heating by merging method have been intensively studied in TS-3/TS-4 and MAST (Although the electron heating mechanism is still unclear, these will be described in Chap.2). Figure.1.4 shows the dependence of the ion heating by merging on

reconnected poloidal magnetic field B_{rec} in TS-3, TS-4 and MAST merging experiments [21]. Through the drastic ion heating, high beta value up to about 50 % and high normalized beta up to 9 have been achieved [18] in TS-3 though the discharge durations were very short.

Thus the ST merging start-up have a potential to be applied as a CS-free start-up method of the ST. However, to realize merging start-up how to generate two initial STs is the most important issue because the initial STs also must be generated without CS. In this section, two ST merging approaches, “merging compression” [22-24] and “double null merging” [19, 25, 26], which are presently mainstream for ST merging start-up method will be explained.

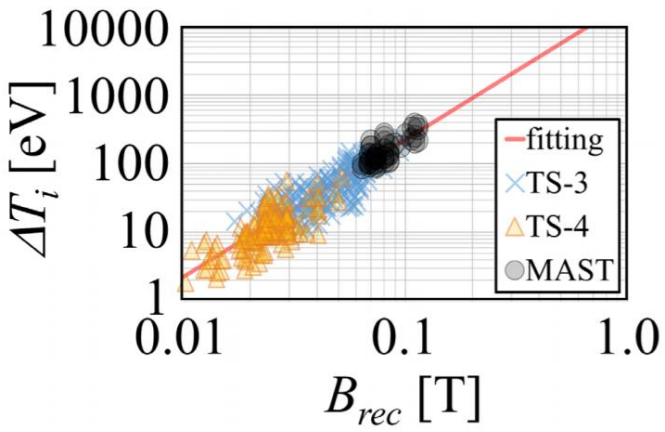

Fig.1.4 The dependence of the ion heating by merging on reconnected poloidal magnetic field B_{rec} in TS-3, TS-4 and MAST merging experiments [21].

1.3.1 Merging compression

Merging compression has been favored in START and MAST. Further, recently this has been employed in ST40 (Tokamak Energy Ltd.) [27] which will have the world highest spec (toroidal field: 3T, plasma current: 2-3MA, plasma temperature: 10 keV will be planed.) due to the potential advantages of this method. Figure 1.5 shows the start-up scenario of ST40 [24]. In this technique, the induction of in-vessel poloidal field (PF) coils (Merging Compression (MC) coils) are used for generating initial tokamak-like plasma. First, when the in-vessel PF coil currents are ramped down, two initial plasmas are generated around upper and lower in-vessel coils. At this moment, these initial plasmas do not satisfy complete tokamak configuration. Secondly, these initial tokamak-like plasmas merge and are pinched off from the PF coils to form a single ST in radially outward region through magnetic reconnection. Then magnetic energy is rapidly converted to kinetic energy or thermal energy by magnetic reconnection. Finally the ST is adiabatically compressed. Then the plasma current and temperature increase by a change in plasma inductance and toroidal magnetic field. Thus the compression ratio which is the ratio between the final plasma geometrical center R_{Geo} and the position of the in-vessel coils for

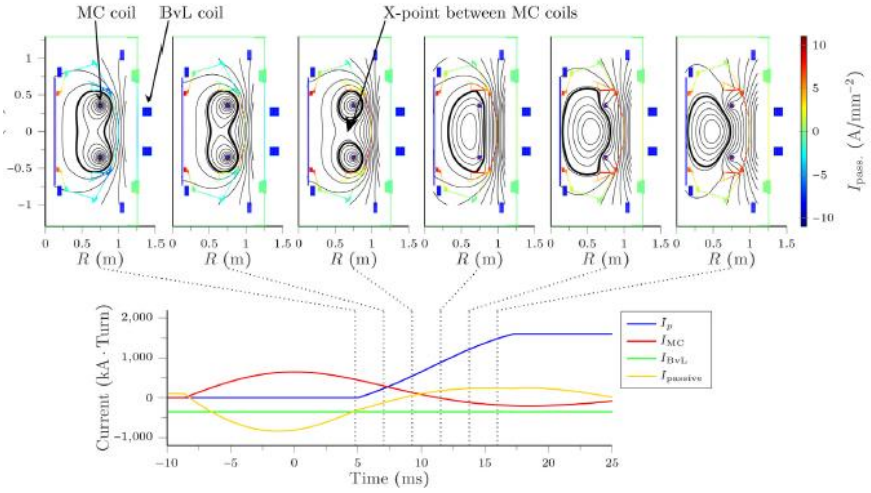

Fig.1.5 The start-up scenario of ST40 [24]

merging compression R_{MC} is important for increasing plasma current as shown in Fig 1.6 [24].

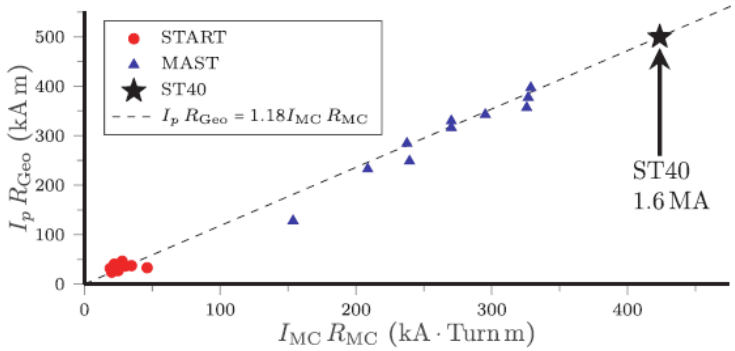

Fig.1.6 Plasma current scaling from START and MAST experimental data [24]

1.3.2 Double null merging

Merging compression is efficient to generate high beta ST dynamically. However this method has two crucial problems in merging compression. First, impurity are released from coil cases around in-vessel coils during start-up phase. Second, such an in-vessel coil can't be set in a future fusion reactor. To overcome these problems two poloidal field-null points in upper and lower regions are used for plasma initiation in double null merging method. This technique has been studied in START and MAST using in-vessel PF coils as well as in the UTST only using ex-vessel PF coils. Figure.1.7 (a) and (b) show schematic view of double null merging in MAST [28] and UTST [25] respectively. First two poloidal field-null points are generated at upper and lower regions by a pair of poloidal field coils. When PF coil currents are ramped down, initial STs are generated at upper and lower null regions. Finally the two STs merge to form single ST through magnetic reconnection as well as merging compression. In START and MAST it is relatively easy

to maintain the initial null fields for a long duration because in-vessel coils are used for generating field-null. However in UTST it is very difficult to generate good field nulls and maintain them for a long period only by ex-vessel coils because eddy current induced by PF coil current ramp down strongly affects formation of the field nulls. Furthermore shielding effect of magnetic field by the eddy current also prevent for effective plasma ramp up by ex-vessel coils. In recent UTST experiment magnetic flux utilization efficiency is only about 3 % because of the shielding by eddy current and the low preionization efficiency. Nevertheless, in UTST the plasma current up to 130kA have been achieved only using ex-vessel coils and experiments for maintaining merging ST by Neutral beam injection (NBI) is starting.

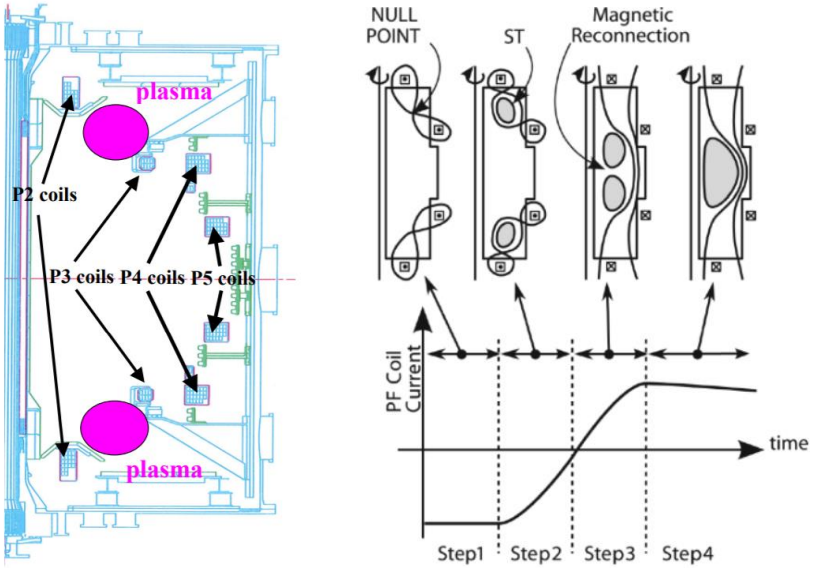

(a) (b)

Fig.1.7 Schematic view of double null merging in (a) MAST [28] and (b) UTST [25]

1.4 Summery

To achieve high-performance ST which can be connected to additional heating by RF or NBI using ST merging it is necessary for optimizing reconnection heating during merging as well as improving the process of initial plasma ramp up. Direct ion heating through magnetic reconnection has been widely researched in TS3/TS4 and START/MAST experiments. However, more extensive investigations especially about electron heating mechanism are necessary to gain a further understanding of the reconnection process in ST merging because electron heating mechanism is still unclear. Next chapter magnetic reconnection which is an ubiquitous phenomena will be simply explained.

Chapter 2

Magnetic reconnection

2.1 Magnetic reconnection

Magnetic reconnection is a ubiquitous phenomenon observed in solar atmosphere, earth's, magnetosphere, nuclear fusion plasmas and so on. Understanding the mechanism of magnetic reconnection is necessary to improve the efficiency of the merging start-up method because magnetic reconnection play a key role in plasma heating during ST merging start-up. Figure.2.1 shows topology of the magnetic reconnection. When plasmas containing anti-parallel magnetic field line approach, the current sheet is induced to prevent approach of the magnetic field line. This current is diffused by some reasons (classical resistivity, anomalous resistivity or other instabilities) and the magnetic field line reconnect at magnetic null point (X-point). Then

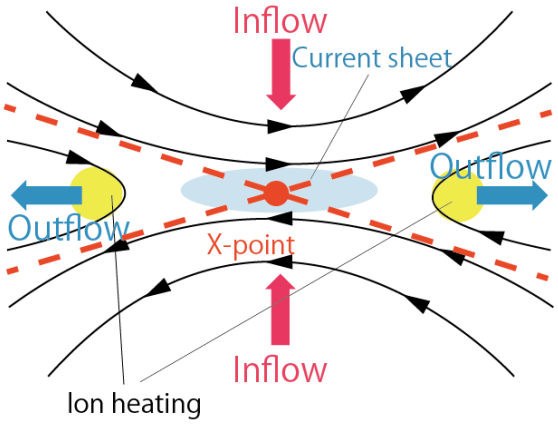

Fig.2.1 Topology of the magnetic reconnection

reconnected magnetic field is pulled out by its own magnetic tension, which cause plasma acceleration. Ions in the plasma are dominantly energized and are heated through some thermalization mechanism in the downstream region [29].

2.1.1 Sweet-Parker reconnection model

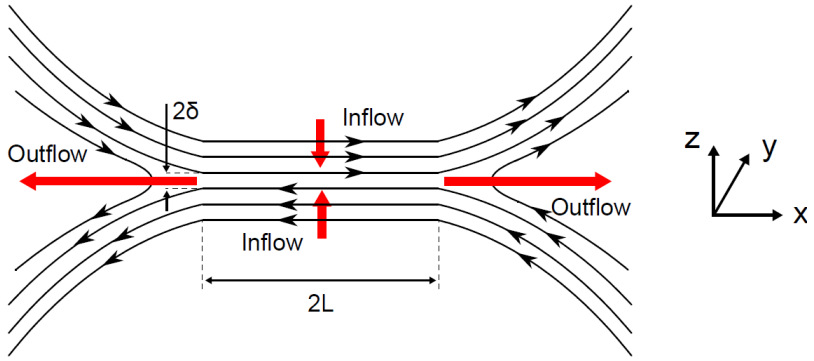

Fig.2.2 Schematic drawing of Sweet-Parker reconnection configuration

The reconnection process has been historically interpreted by using two-dimensional steady magnetohydrodynamics (MHD) model called “Sweet-Parker” model [30]. Fig.2.2 shows schematic drawing of Sweet-Parker reconnection configuration. Sweet and Parker proposed elongated diffusion region as shown in Fig.2.2. The electric field $\mathbf{E}$ is given by the resistive MHD form of classic ohm's law as

$$\mathbf{E}+\mathbf{v}\times\mathbf{B}=\eta\mathbf{j} \tag{2.1}$$

Since there are no B_x and B_z at the X point, eq.(2.1) is simplified as

$$E_y=\eta j_y \tag{2.2}$$

On the other hand ideal MHD condition holds in for upstream and downstream regions, eq.(2.1) is re-written as

$$-E_y = v_{in} B_{in} = v_{out} B_{out} \tag{2.3}$$

where $B_{in} = B_x$ is the reconnecting magnetic field in the upstream region and $B_{out} = B_z$ is the magnetic field in the downstream region. Then using eq.(2.3) inflow velocity is given by $E \times B$ drift velocity as

$$v_{in} = \frac{E_y}{B_{in}} \tag{2.4}$$

Next, Ampere's law

$$\mathbf{j} = \frac{\nabla \times \mathbf{B}}{\mu_0} \tag{2.5}$$

is applied to the reconnection region. In the low velocity approximation, displacement current can be neglected. So eq.(2.5) can be reduced to

$$j_y = \frac{B_{in}}{\mu_0 \delta}. \tag{2.6}$$

Then using eq.(2.2), (2.4) and (2.6) inflow velocity is derived as

$$v_{in} = \frac{\eta}{\mu_0 \delta} \tag{2.7}$$

Considering conservation of mass of inflow and outflow regions

$$v_{in} L = v_{out} \delta . \tag{2.8}$$

By substituting eq.(2.8) to eq.(2.7)

$$v_{in} = \sqrt{v_{out} \frac{\eta}{\mu_0 L}}. \tag{2.9}$$

Furthermore considering the balance of energy between in inflow and outflow region

$$\frac{B_{in}^2}{2\mu_0} = \frac{\rho v_{out}^2}{2}. \tag{2.10}$$

where ρ is mass density in outflow region. In this way outflow velocity is given as

$$v_{out} = v_A = \frac{B_{in}}{\sqrt{\mu_0 \rho}} \tag{2.11}$$

where v_A is the Alfven velocity. So using eq.(2.9) reconnection rate is given as

$$\frac{v_{in}}{v_A} = \frac{1}{\sqrt{S}} \tag{2.12}$$

where S is the Lundquist number,

$$S = \frac{\mu_0 L v_A}{\eta}. \tag{2.13}$$

However, the Sweet-Parker model can not explain the short reconnection time scale actually observed in solar flares or laboratory reconnection experiments. The fast reconnection mechanism is one of the most important issues in the magnetic reconnection research field.

1.1.2 Two-fluid effect of the reconnection current layer

Recent numerical and experimental studies suggested that two-fluid effect is necessary to be considered [31] when the length of the diffusion region scale approaches to the ion inertial length, $d_i = c/\omega_{pi}$, scale. Here the two-fluid ohm's law is described as

$$\mathbf{E} + \mathbf{v} \times \mathbf{B} = \eta \mathbf{j} + \frac{1}{ne} \mathbf{j} \times \mathbf{B} - \frac{1}{ne} \nabla \mathbf{P} + \frac{m_e}{ne^2} \frac{\partial \mathbf{j}}{\partial t}, \tag{2.14}$$

where second term of the RHS is called Hall term, third term of the RHS describes the effect of the electron pressure gradient and fourth term of the RHS describes the effect of electron inertia. When the electron mean free path becomes comparable to the current sheet, Hall term especially becomes dominant because electrons are magnetized but ions are weekly magnetized in the vicinity of the X point. Then electron and ion flow patterns are decoupled as shown in Fig.2.3

[31]. When the Hall term is dominant, characteristic quadrupole out-of-plane magnetic field is created by the Hall current. In any simulations using a Hall MHD code, a hybrid code, or a PIC code, the Hall term is the primary cause to promote magnetic reconnection.

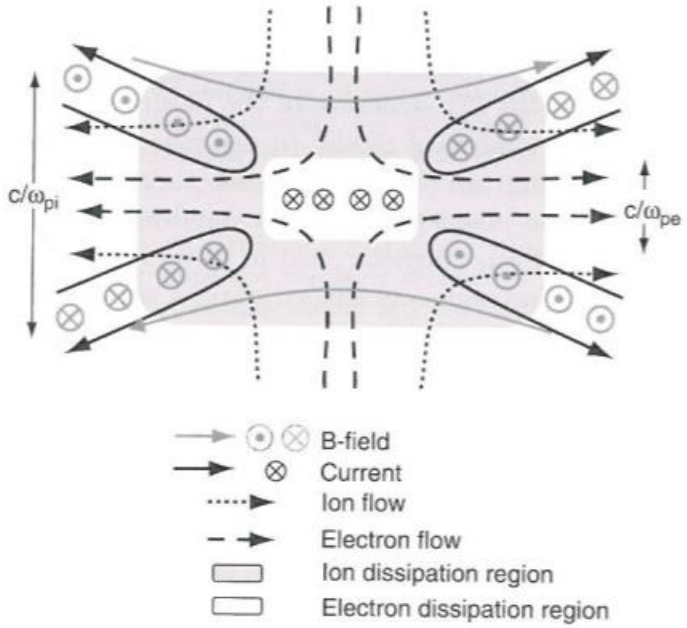

Fig.2.3 Schematic drawing of two-fluid dynamics of reconnection current layer [31]

2.1.3 Magnetic reconnection in the presence of guide field

In this thesis the author focus on the study of the guide field reconnection because reconnection in ST merging has a strong guide field, which corresponds to the toroidal field normal to reconnecting magnetic field. In MHD reconnection framework it is considered that guide field simply reduce the reconnection rate [32, 33] because it enhances magnetic pressure inside the current sheet. As predicted in MHD reconnection framework, in ST merging ion heating energy surely decreased in the presence of the strong guide field. However, fortunately ion heating energy

and reconnection rate just have weak dependence on the guide field [34] and the ion heating is still effective even in high-q tokamak merging studied in START/MAST device (UKAEA) and UTST.

Recent results from the PIC simulation studies predict that electron and ion in-plane flow patterns become asymmetric in guide field reconnection as shown in Fig.2.4 [35] whereas the flow patterns are symmetry in non-guide field reconnection. The flow pattern of the electrons can be explained by the geometry of the magnetic field line. Figure.2.5 shows the three dimensional geometry of the magnetic field line in guide field reconnection. Electrons are accelerated along the field lines by reconnection electric field around the X point and flow out on a particular pair of the separatrix forming the asymmetric profile. As a result charge separation occurs and the quadrupole structure of the electrostatic potential finally creates asymmetric ion flow.

The local electron acceleration by the parallel electric field is predicted as one of the characteristic of the guide field reconnection in PIC simulation. Fig.2.6 shows the spatial profile of parallel electron velocity obtained by the PIC simulation [35]. In the presence of the guide field electrons are effectively accelerated directly by reconnection electric field around the X point. Furthermore the electron velocity distribution is non-Maxwellian and energetic electrons are generated at the region around the X point.

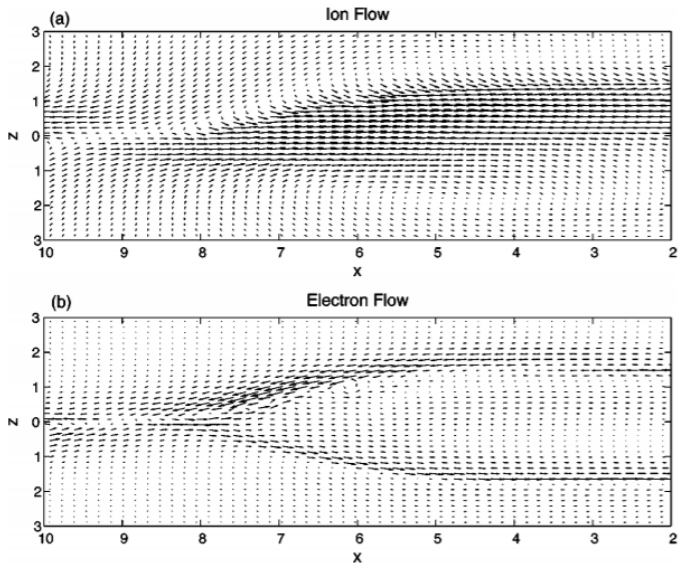

Fig.2.4 The ion and the electron in-plane flow patterns in the guide field reconnection [35]

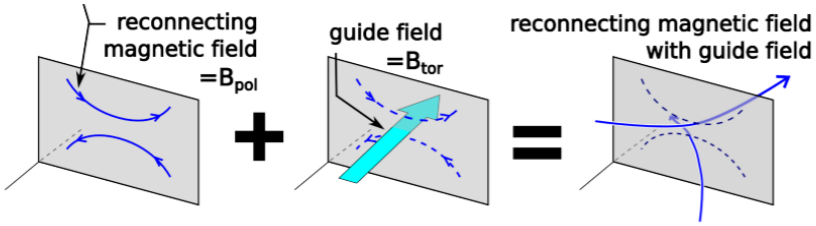

Fig.2.5 The three dimensional geometry of the magnetic field in the guide field reconnection

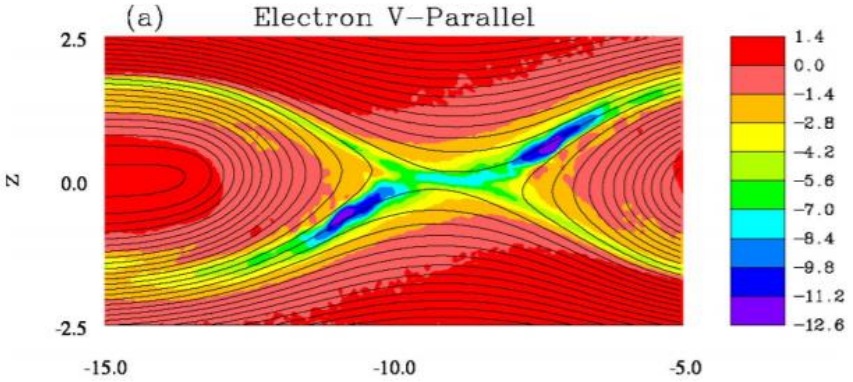

Fig.2.6 The profile of parallel electron velocity in the guide field reconnection [35]

2.1.4 Characteristic electron heating in ST merging

Although electron energization mechanism has not experimentally verified yet, remarkable electron heating was observed in MAST merging experiment through guide field reconnection. Fig.2.7 shows the result of Thomson scattering measurement in MAST merging experiment [36]. In Fig.2.7 local electron heating was observed after magnetic reconnection. In ST merging only the poloidal magnetic field energy is released and contributes to the energy conversion of the magnetic reconnection. However, in MAST experiments the peak value of the electron temperature depended on the value of toroidal magnetic field, namely, the guide field.

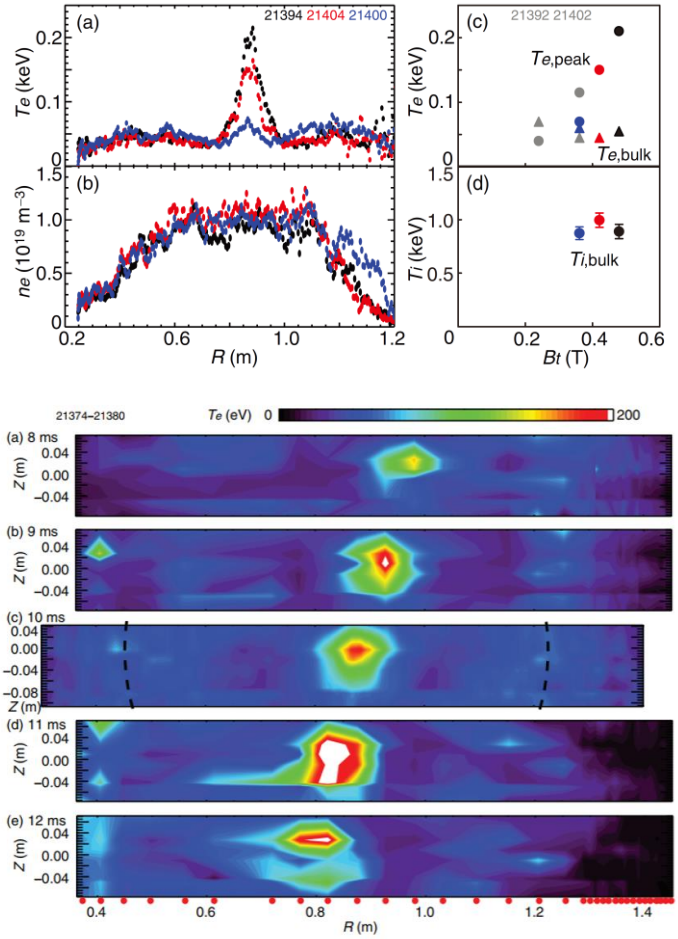

Fig.2.7 Result of Thomson scattering measurement in MAST experiment [36]

To investigate the mechanism of the local electron heating, Hall MHD simulation of the ST merging was performed. Figure.2.8 shows the profile of the electron temperature during ST merging in Hall MHD simulation [37]. The electron temperature has hollow profile after merging in contrast to the centrally-peaked profile as shown in Fig.2.8. Thus the results from Hall MHD simulation do not explain the experimental observations possibly because it does not include the kinetic effect of particles.

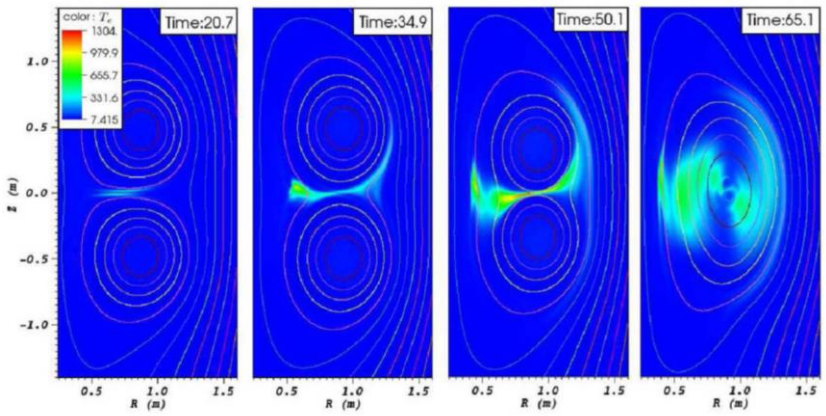

Fig.2.8 The predicted electron temperature profile during merging experiments by Hall MHD simulation [37]

Chapter3

Objectives of this thesis

ST merging start-up is one of the potential candidates of the CS-free start-up methods because of the rapid plasma heating through magnetic reconnection and resulting high beta characteristic. As for reconnection heating effects, direct ion heating during ST merging have been widely researched. The previous studies have shown that the ion heating can be estimated from the value of reconnecting magnetic field which depend on initial plasma current. However, electron heating mechanism during merging is still unclear although characteristic electron heating was observed after merging in MAST merging operations. Hence, this thesis primarily addressed the electron energization mechanism during ST merging start-up. In ST merging, which includes the reconnection event in the presence of the guide field, characteristic electron acceleration is predicted by numerical studies as explained in Chap.2. As objectives of this thesis, the author experimentally investigated;

- whether the electrons are accelerated in parallel direction by reconnection electric field near the X point or not
- 2D profile of the accelerated electrons on the poloidal cross section

using the UTST merging experiment.

Furthermore, it is also important to investigate how the accelerated electrons affect the final ST equilibrium after merging, particularly the electron temperature. However, in the present UTST merging setup the electron heating efficiency during merging start-up cannot be evaluated quantitatively partly because the magnetic probe array inside plasma prevents electrons from heating. To investigate electron heating effect through magnetic reconnection quantitatively the plasma shape and position measurement without using magnetic probe array inside plasma is necessary. Then another objective of this thesis is

- realizing plasma shape reconstruction of the merging STs only based on the magnetic sensors outside plasma.

These will be explained in Chap.6 and Chap.7, respectively.

Chapter 4

UTST device

4.1 Overview of UTST device

The University of Tokyo Spherical Tokamak (UTST) device was constructed in order to demonstrate “double null merging” start-up without using internal PF coils. As shown in Chapter 1, other merging devices has already demonstrated ST merging start-up scheme by using internal PF coil, but the internal coils which directly face the plasma are not acceptable in the future fusion reactor. When we consider the fusion reactor using merging method, heat and neutron load on internal coil largely spoils feasibility of fusion power plant. Hence, UTST is designed to have all PF coils located outside the vacuum vessel and bears an important part of realizing plasma merging method for fusion reactor. Figure.4.1 shows UTST device photograph and Table.4.1 shows major parameters of UTST device and merging experiment. Table.4.2 shows the coil parameters and Fig.4.2 shows cross section of UTST device. Table.4.2 shows the coil parameters, Table.4.3 shows the capacitor banks parameters and Fig.4.2 shows the poloidal cross section of UTST device.

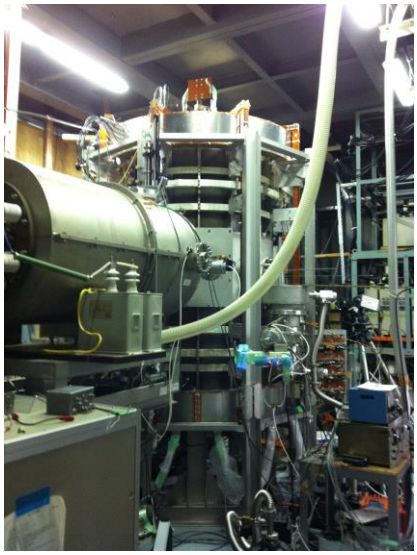

Fig.4.1 UTST device

Table.4.1 Major parameter of UTST device and merging experiment

Chamber radius	0.7m (midplane) 0.6m (top & bottom)
Chamber height	2.0m
Toroidal B field (guide field)	< 0.3T
Poloidal B field (reconnection field)	< 0.015T
Major radius	0.35 m
Aspect ratio	1.3
Plasma current	130kA (w/o CS)
Ion temperature	50eV
Electron temperature	30eV
Electron density	$5\times10^{19}\mathrm{m}^{-3}$

Table.4.2 Coil parameters

Coil	Z(mm)	R(mm)	Turns	Major use
TF		1000	16	Applying the external toroidal magnetic field
PF1(upper)	1100	200	8	Pushing the initial STs to the midplane
PF1(bottom)	-1100	200	8	Pushing the initial STs to the midplane
PF2(upper)	800	685	3	Generating the initial STs by flux swing
PF2(bottom)	-800	685	3	Generating the initial STs by flux swing
PF3(upper)	675	750	8	Fast adjustment of equilibrium magnetic field
PF3(bottom)	-675	750	8	Fast adjustment of equilibrium magnetic field
PF4(upper)	500	685	3	Generating the initial STs by flux swing
PF4(bottom)	-500	685	3	Generating the initial STs by flux swing
CS		83.5	110-440	Current drive

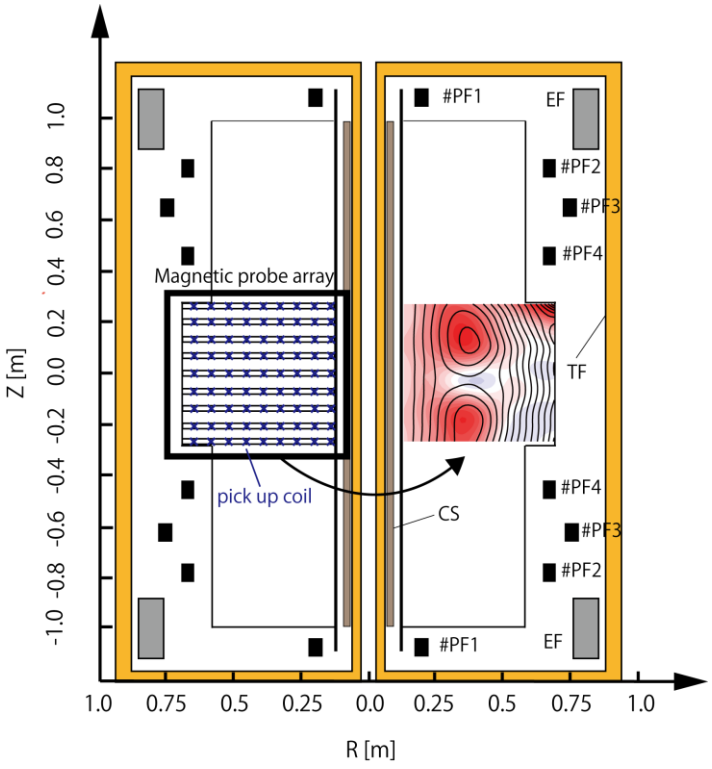

Fig.4.2 The poloidal cross section of UTST device

4.2 Double null merging operations in UTST

Two types of double null merging operations have been demonstrated in UTST. In the early UTST merging operations PF1 and PF4 coils (PF#2 in Fig.4.3) which are connected in parallel to capacitor banks have been used to generate initial field nulls at upper and bottom region and apply inductive electric field as shown in Fig.4.3 [25]. In this operation relative wide field nulls were generated at the area between PF1 and PF4 coils. However it was difficult to induce enough poloidal flux at the null point because maximum initial poloidal flux at the null points which determines the capability of initial plasma current drive was limited mainly by the performance of PF1 coils because it is difficult to produce large magnetic flux by a small radius coil and a fast capacitor bank.

To overcome this problem, in the recent UTST merging operations, PF2 and PF4 coils which are also connected in parallel to capacitor banks have been used to generate initial field nulls as shown in Fig 4.4 [19]. In this operation the eddy current plays an important role to form initial field nulls because the internal magnetic field is generated by the combination of the PF2 coil current, the PF4 coil current and the eddy current on the vacuum vessel. By this improvement more initial poloidal flux was able to be stored at the null points than in the previous operations and the plasma current up to 130kA was achieved only using ex-vessel coils. However, there are still rooms for improvement in UTST merging operations.

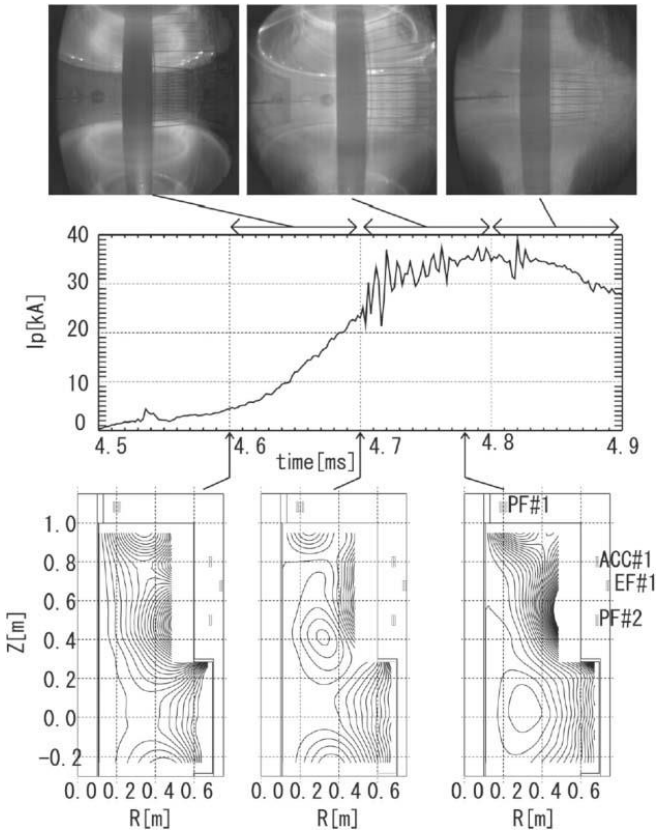

Fig.4.3 UTST merging operation using PF1 and PF4 coils (PF#2 in this figure) [25]

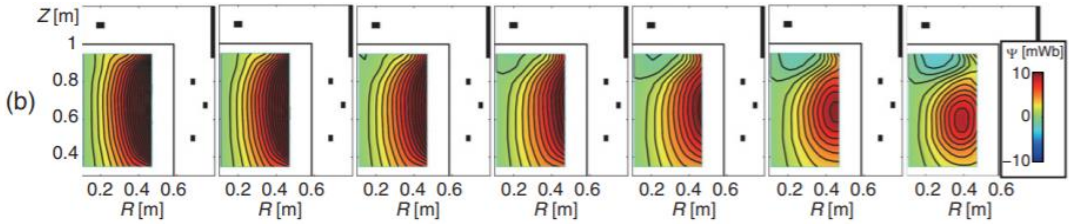

Fig.4.4 UTST merging operation using PF2 and PF4 coils [19]

4.3 Washer gun

In inductive start-up, preionization is important for efficient flux consumption. Especially in inductive start-up only using ex-vessel PF coils like UTST merging start-up reduction of the breakdown time is one of the important issue because it is difficult to maintain field nulls over a long period.

In ohmic discharge of tokamaks, preionization is usually given by electron cyclotron heating (ECH) system. However, in UTST discharges preionization is carried out with washer guns. Figure.3.5 shows a picture of washer gun and an interior of the structure. When the high voltage is applied between anode and cathode, arc discharge is occurred between the electrodes along inner surface of the ceramic washers. Then plasma is injected from the anode along the background magnetic field line. Since in double null merging operation two private poloidal fluxes are generated to form two initial STs, UTST device has two washer guns located at upper and bottom region to inject plasmas into each field null area as shown in Fig.4.5. The preionization by washer gun is advantageous from viewpoints that high density plasma can be provided at the low producing cost of the gun while impurity are released from metal washers.

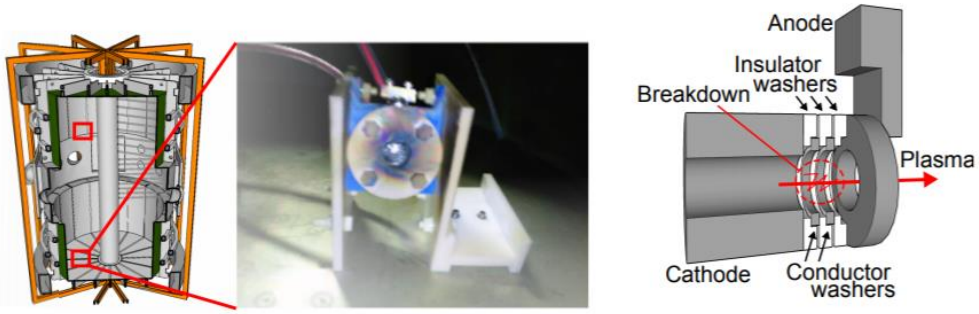

Fig.4.5 A picture of washer gun and an interior of the structure

4.4 Magnetic probe array

To observe magnetic reconnection structure during ST merging, two-dimensional array of pick up coils is employed in UTST. The magnetic probe array has 81 channels in the central section to measure the magnetic field Bt and Bz directly inside the vacuum vessel in the middle region (-0.24 ≤ z ≤ 0.24m). The poloidal flux and toroidal current density can be derived from the measured magnetic field with assumption of toroidal symmetry and a perfect conductor wall (Poloidal flux is zero on the vacuum vessel wall.). The location of pickup coils is shown in Fig4.2. Poloidal magnetic flux, current density and toroidal electric field are calculated by the following formulas

$$\Psi\left(R,t,z\right)=2\pi\int_{R_0}^{R}B_z(\rho,t,z)\rho d\rho \tag{4.1}$$

$$jt\left(R,t,z\right)=-\frac{1}{\mu_0}\left(\frac{1}{2\pi R}\frac{\partial^2\Psi(R,t,z)}{\partial z^2}+\frac{\partial B_z(R,t,z)}{\partial R}\right) \tag{4.2}$$

$$Et\left(R,t,z\right)=-\frac{1}{2\pi R}\frac{d\Psi(R,t,z)}{dt}\ . \tag{4.3}$$

Poloidal magnetic flux and current density are calculated in order to know the topology of merging and the location of reconnection current layer, respectively. The reconnection electric field appears as toroidal electric field in UTST merging experiment. This is one of the most important parameter of electron acceleration. Toroidal electric field is calculated from the time derivation of the poloidal magnetic flux at the X point.

4.4.1 Evils caused by inserted magnetic probe array

The magnetic probe array is convenient for reconnection research. On the other hand the magnetic probe array is intended to disturb maintaining the plasma current and heating electrons. Figure.4.6 shows plasma current and soft X-ray signals measured by SBD (explained in Chap.5) with different X-ray absorption filters, 3μm Al and 1μm mylar foil, and same line-of-sight in the merging operation assisted by CS coil current drive with the magnetic probe array (black line) and without the magnetic probe array (red line). As shown in the top panel of Fig.4.6, the plasma current with magnetic probe array decay faster than that without magnetic probe array. The middle and bottom panels of Fig.4.6 show that the soft X-ray signal (1μm mylar foil) remarkably increased in the case without magnetic probe array even though the soft X-ray signal (3μm Al foil) was almost same in the both case. Then Fig.4.7 shows the dependence of electron temperature on the ratio between two soft X-ray signals when electron density and temperature profile are spatially constant. Fig.4.7 shows on one-to-one correspondence with the electron temperature and the signal ratio when the electron temperature is less than 300eV. This suggest that electron temperature remarkably increased in the case with magnetic probe array because in the case without magnetic probe the signal ratio is larger than that with the magnetic probe.

Recent UTST experiments suggested that the electrons are effectively accelerated in the parallel direction along the magnetic field line by the reconnection electric field during merging (The detail will be explained in Chapter.6) and energetic electrons are generated. To investigate how electron acceleration take place during the guide field reconnection and to optimize the merging start-up without use of internal magnetic measurement are essential.

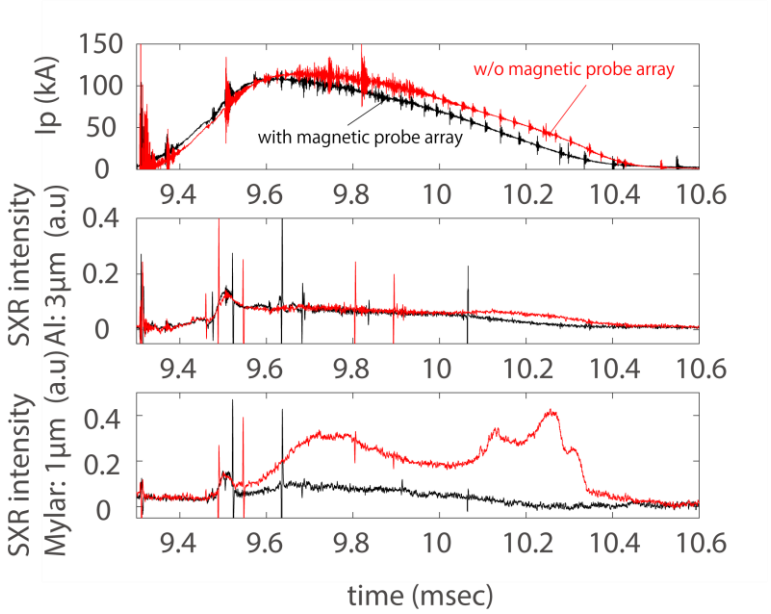

Fig.4.6 Plasma current and soft X-ray signals measured by SBD (explained in Chap.5) with different X-ray absorption filters, 3μm Al and 1μm mylar foil, in the merging operation assisted by CS coil inserting the magnetic probe array (black line) and without the magnetic probe array (red line).

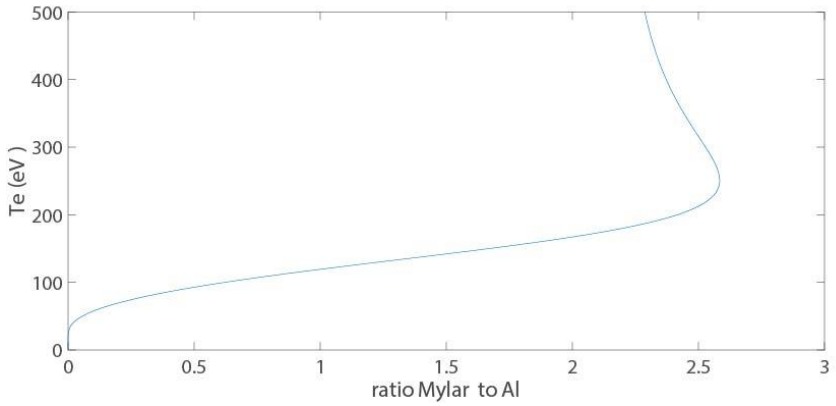

Fig.4.7 The dependence of electron temperature on the ratio between two soft X-ray signals (3μm Al and 1μm mylar foil) when electron density and temperature profile are spatially constant.

Chapter 5

Soft X-ray measurement system

5.1 Surface barrier detector

Surface barrier detector (SBD: Ortec model CR-017-050-10) is widely used to observe soft X-ray. In this study SBD (Ortec model CR-017-050-10) was employed to observe soft x-ray by bremsstrahlung emission from fast electrons accelerated during magnetic reconnection. The SBD is a diode covered with thin aluminum (0.15μm) rectifying contact on p-type Si and have good sensitivity over the energy range of soft x-ray (< 20keV). Thickness of the Si dead layer is 0.01μm. Soft X-ray from the reconnection X-point region is detected by two SBDs which have tangential line-of-sight with radius of 35 cm. Pinholes with aperture diameter of φ4mm are equipped in front of SBDs. Fig5.1 shows the cross section of the vacuum flange for soft X-ray measurement. Fig.5.2 shows the location of SBD line of sight. The SBDs have viewing field which covers the reconnection region. Furthermore, X-ray absorption filter is equipped in front of the SBD to eliminate photon with low energy. Transmittance of polycarbonate X-ray absorption filter with consideration for the rectified aluminum and dead layer of Si is calculated by using database of NIST [38] as shown in Fig.5.3. Note that the response of SBD decreases for higher photon energy because the high energy photons in hard X-ray range pass through the dead layer. Detected current by SBD is converted to voltage signal by an I/V converter and amplified by a preamplifier. Furthermore, a buffer circuit is also set next to the preamplifier to reduce the effect of long transmission cable and keep good frequency response. Figure. 5.4 shows the circuit of the I/V

converter, preamplifier and buffer circuits.

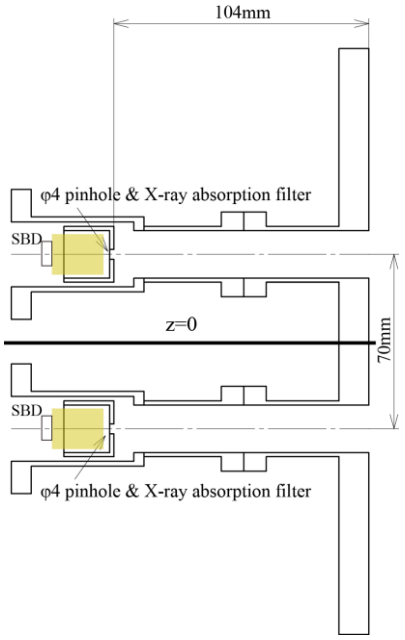

Fig.5.1 Cross section of flange for SBD measurement

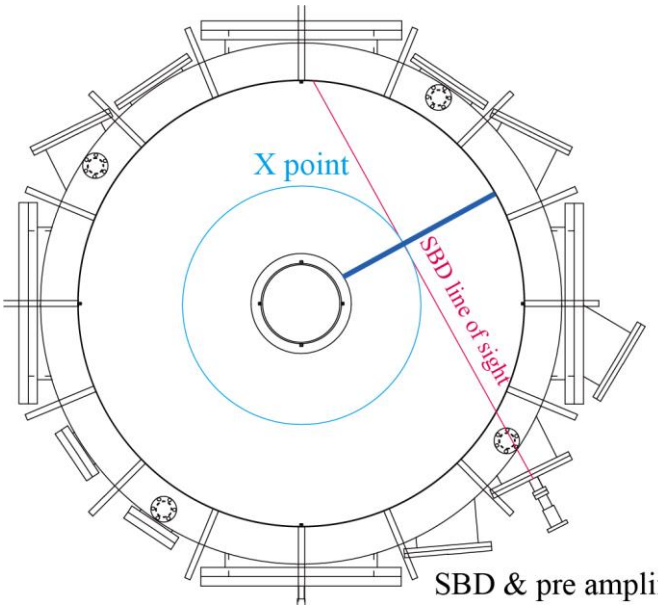

Fig5.2 Locations of SBD line of sight and X point radius

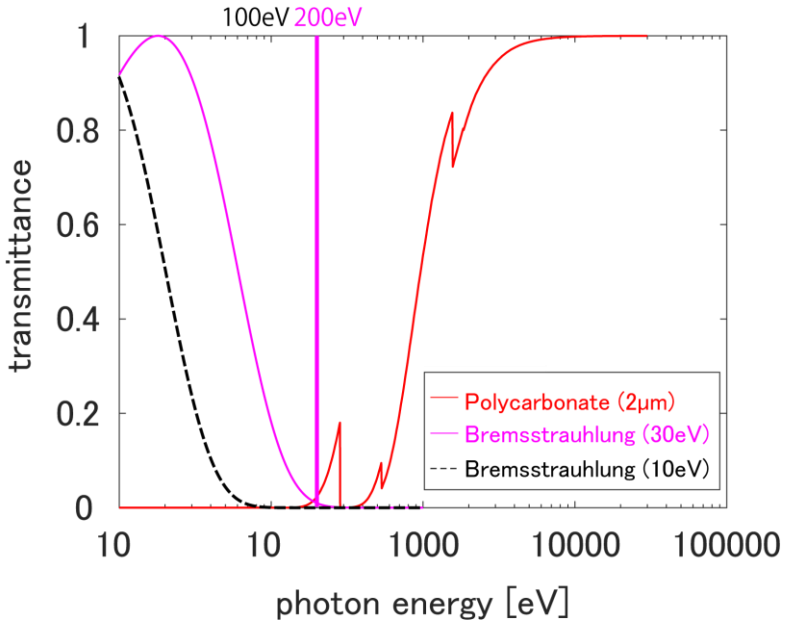

Fig.5.3 Transmittance of X-ray absorption filter containing rectified aluminum and dead layer of Si [38]

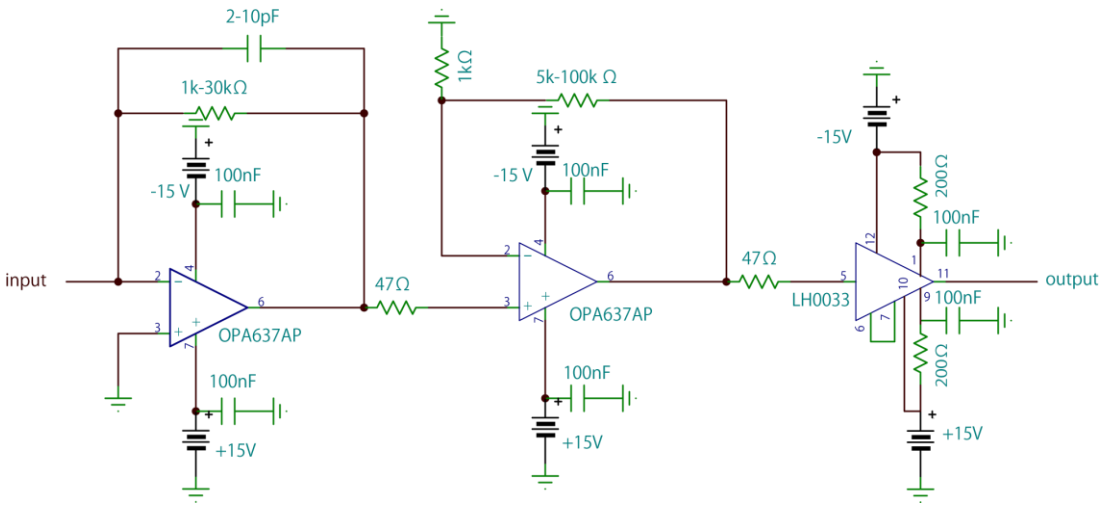

Fig.5.4 Circuit diagram of I/V converter, preamplifier and buffer

5.2 Soft X-ray imaging system

To detect two dimensional soft X-ray image the assembly of micro channel plate (MCP) and phosphor (HAMAMATSU PHOTONICS K. K: F2222-21P) is used. The MCP consists of two dimensional array of a great number of glass capillary tube. When the high voltage is applied between input side electrode and output side electrode, each tube detects X-ray and multiplies photoelectrons. Figure.5.5 shows the schematic view of the soft X-ray imaging system. The soft X-ray imaging system consists of a pinhole, MCP and phosphor plate. Firstly when the soft X-ray is incident on the surface of the MCP, photoelectrons are emitted. Secondary the emitted electrons are accelerated by the strong electric field between electrodes and multiplied every time when hitting the inside wall of the capillary tubes in the 2 stage of MCP. Finally the multiplied electrons hit the phosphor plate and are converted into visible image on the plate. The type of phosphor screen is P46 which is composed by $Y_3Al_5O_{12}$:Ce and the decay of light intensity is 0.2-0.4μsec.

The visible images on the phosphor plate were recorded by fast camera, SA-Z (Photron). Thin mylar foil (1μm) was equipped on the pinhole to observe the bremsstrahlung caused by tail components of the electron energy distribution function. The transmittance of mylar (polyester) foil (1μm) and the bremsstrahlung expected to be emitted from bulk electrons in UTST are shown in Fig.5.6 [38].

As shown in Fig. 5.5 high voltage pulses are applied between MCP input side electrode and output side electrode as well as the phosphor screen and GND (MCP output side electrode) only for 100-200μsec to avoid unexpectedly applying higher voltage than the rated voltage because large loop voltage is induced by poloidal field coil current swing in merging start-up. The high voltage pulse generator consists of high voltage power supply and MOSFET as shown in Fig.5.7.

The vacuum chamber of the soft X-ray measurement system is evacuated to less than 1.3×10^{-4} Pa by a vacuum pumping system separated from the UTST main vacuum components. Vacuum baking by nichrome wire is effective to evacuate the stored gas in the capillary tube of MCP. It is important for achieving good S/N because such a stored gas can cause weak discharges inside the

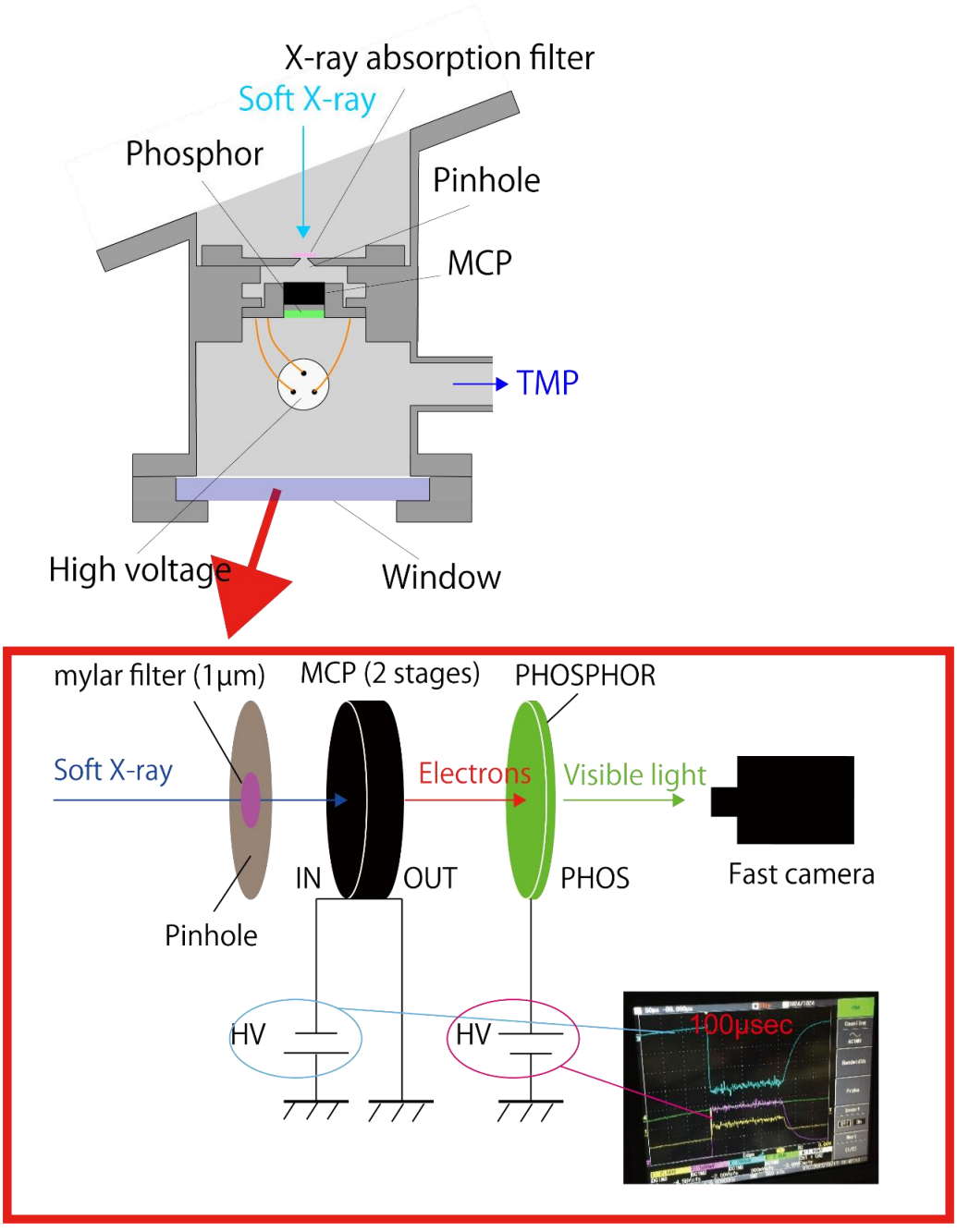

Fig.5.5 The schematic view of the soft X-ray imaging system

capillary tubes and make noises.

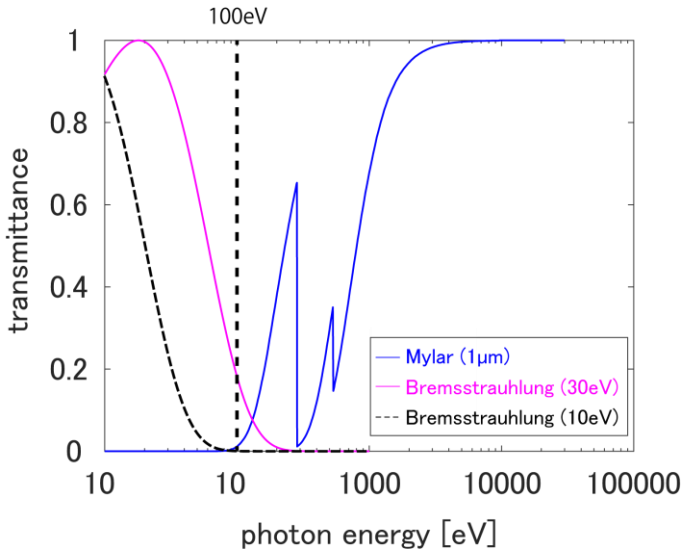

Fig.5.6 The transmittance of mylar foil (1μm) and the bremsstrahlung expected to be emitted from bulk electrons in UTST [38]

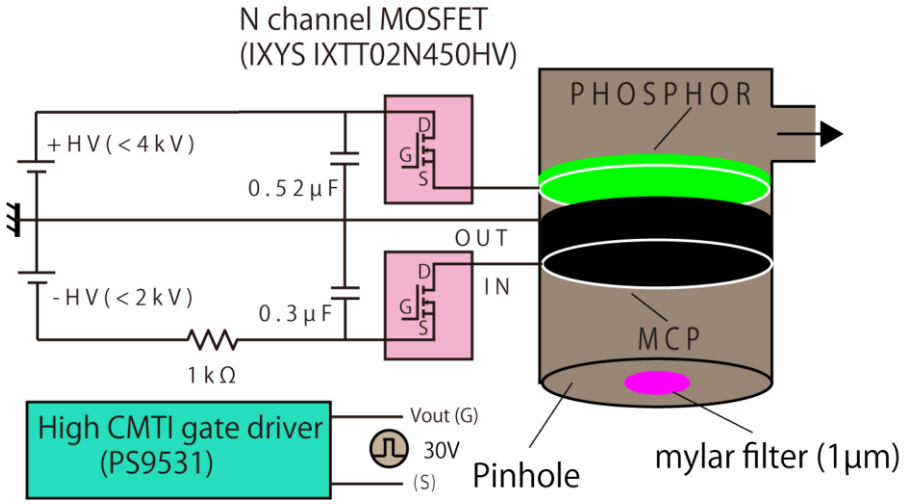

Fig.5.7 Circuit of high voltage pulse generator

5.2.1 Image correction

Relative detection efficiency of MCP depends on the incident angle of soft X-ray from the axis of capillary tube. When the incident soft X-ray is parallel to the axis of capillary tube, the relative detection efficiency of MCP decreases. Figure.5.8 and Fig.5.9 show the dependence of relative detection efficiency on soft X-ray incident angle [39] and relative detection efficiency profile son the MCP when the photon energy is in soft X-ray range, respectively. As shown in Fig.5.9 the hole-shaped low relative detection efficiency area is slightly off-center because each capillary tube is set on the angle of 8 degree with the MCP surface normal, so called bias angle. To fill the dark hole of the soft X-ray images, the images need to be retouched by a correction factor.

Furthermore, geometrical effect of the solid angle of observation is also important. In the pinhole camera the solid angle of observation usually differs between detector channels. So when the local emission profile is reconstructed by some kind of tomographic techniques based on the profile of line integrated signals, the geometrical effect must be considered. For simplification, the 3D solid angle is usually approximated as 2D solid angle or 1D line of sight. In line of sight approximation geometrical factor is described as

$$f_{geo} = \frac{A_{\det} A_{pin}}{4\pi d^2} \cos^4 \alpha \,, \tag{5.1}$$

where $A_{\det}$ and A_{pin} are the aresa of detector channel and pinhole respectively, d is the distance between the pinhole and the detector, α is angle between the line of sight and normal to the pinhole. In the soft X-ray imaging system, the area of detector cannel and of pinhole and the distance between the pinhole and the detector are constant. Finally $\cos^4 \alpha$ effect remains.

Strictly speaking, the effective thicknesses of the absorption filters depend on $1/\cos\alpha$ if the filters are flat. This effect does not depend only on geometrical effect but also on electron velocity

distribution function. In this thesis, the effective thickness are ignored because dependence on $1/\cos\alpha$ is less than 8 % even at the edge of the MCP.

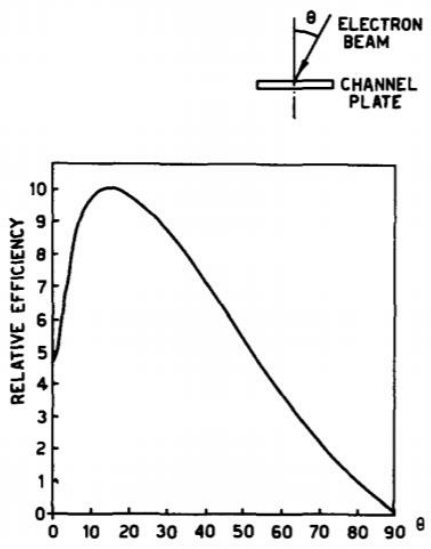

Fig.5.8 The dependence of relative detection efficiency on soft X-ray incident angle [39]

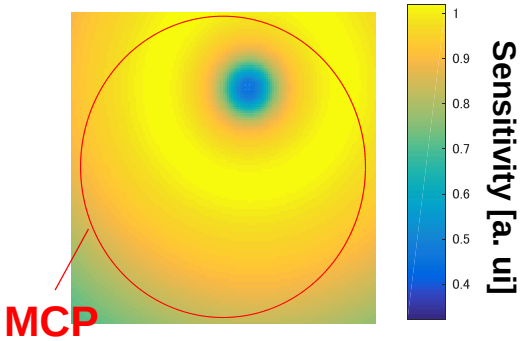

Fig.5.9 The relative detection efficiency on the MCP when the photon energy is in soft X-ray range

5.2.2 Abel inversion

2D soft X-ray profiles on the poloidal cross section are reconstructed by Abel inversion technique. Abel inversion is one of the computer tomographic technique to identify the radial profile based on the axisymmetric assumption. When the toroidal axisymmetric emission are assumed as shown in Fig.5.10, line integrated intensity is described as

$$I(y) = 2\int_0^{\sqrt{R^2-y^2}} \varepsilon(r)dx = 2\int_y^R \frac{\varepsilon(r)rdr}{\sqrt{r^2-y^2}}, \tag{5.2}$$

and the local emission profile can be obtained from eq.(5.2) as

$$\varepsilon(r) = -\frac{1}{\pi}\int_r^R \frac{dI(y)}{dy}\frac{dy}{\sqrt{y^2-r^2}}. \tag{5.3}$$

As shown in eq.(5.3), the radial profile can be obtained only by the profile of the line integrated intensity in y direction.

In this thesis 2D the soft X-ray profile are reconstructed using almost horizontal channels of soft X-ray imaging system which are tilted within the range up to 4° relative to the horizontal surface.

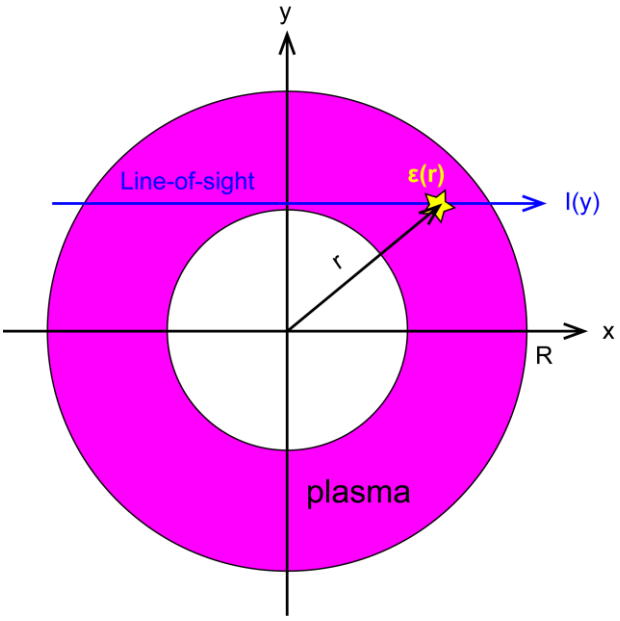

Fig.5.10 The coordinate system of the Abel inversion

Chapter 6

Verification of electron acceleration mechanism during spherical tokamak merging

6.1 Correlation between soft X-ray intensity and effective electric field

In the ST merging experiment, in which a strong toroidal magnetic field is applied, the reconnection electric field in the toroidal direction becomes field aligned near the X-point where the poloidal magnetic field is negligible. The typical ratio of the toroidal (guide) magnetic field to poloidal (reconnection) magnetic field is 10-20 in the UTST experiment, which is much higher than those in previous TS-3/4 experiments or numerical studies. This is a unique feature of the UTST merging experiment that can provide remarkable electron acceleration near the X-point.

First, soft X-ray emission from the reconnection region was observed by using SBD detector as described in Chap.5. Soft X-ray measurement line of sight is shown in Fig. 5.2. Figure 6.1 shows the typical waveforms of reconnection parameters such as (upper) the reconnected magnetic flux, (middle) the reconnection electric field, and (bottom) the soft X-ray signal measured by SBD measurement system (For details, see Chap. 5.) during magnetic reconnection and their corresponding poloidal flux surfaces. Sharp soft X-ray (>200eV) bursts were observed only during magnetic reconnection with a roughly good correlation with the reconnection electric field at the X-point. There are two possible origins of the soft X-ray bursts: thermal and non-thermal electrons generated during reconnection. The Thomson scattering measurement revealed that the electron temperature in the UTST merging experiment was up to 30 eV [41],

which is much lower than the absorption edge of the filter used in the present study, as shown in Fig.5.3. Therefore, it is considered that non-thermal fast electrons accelerated by the field-aligned electric field account for the observed soft X-ray emission.

The intensities of the soft X-ray bursts were depended both on the reconnection electric field and toroidal magnetic field in the UTST merging experiment. Figure 6.2 shows the dependence of the soft X-ray intensity on $E_t\left(B_t/B_p\right)$ under the condition that $B_p = 0.01\mathrm{mT}$. The soft X-ray intensities exhibited a clear increasing trend with $E_t\left(B_t/B_p\right)$, suggesting that the efficiency of electron acceleration can be expressed by the effective electric field $E_{eff} \sim E_t\left(B_t/B_p\right)$ near the X-point region in analogy with torus plasma breakdown, where electrons near the null point are effectively accelerated [42].

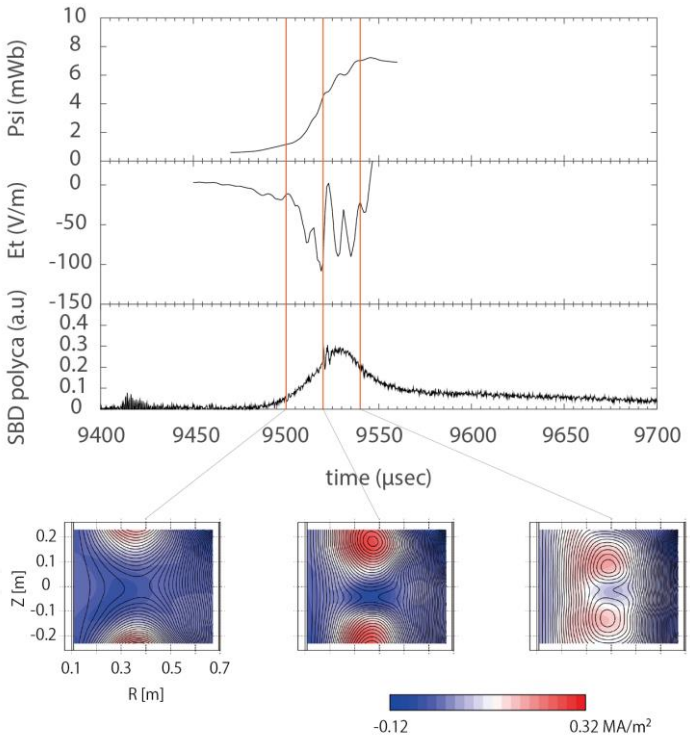

Fig. 6.1. Evolution of reconnection parameters: (top) reconnection magnetic flux, (middle) toroidal electric field, and (bottom) soft X-ray (polycarbonate: 2 μm) during reconnection. Corresponding poloidal flux surfaces are also shown [40].

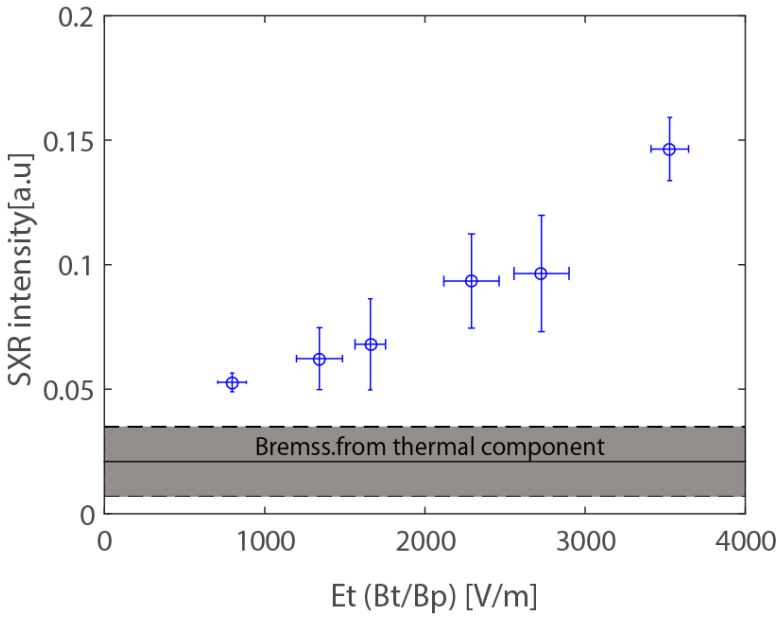

Fig. 6.2. Dependence of soft X-ray intensity on E_{eff} [40].

6.1.1 Evaluation of electron acceleration by 0D model

Based on the experimental results presented above, possible mechanisms to generate energetic electrons are now discussed. To quantitatively evaluate electron acceleration, a simple 0D model considering the acceleration period was developed. In this model, electrons are accelerated along the total magnetic field $B_t + B_p$. Because an acceleration region projected on the poloidal cross section is limited by the half length of a reconnection region L, the electrons can stay inside the acceleration region while their travel length projected to poloidal plane is smaller than L, i.e., the total travel length is defined as $L_t = L\left(B_t^2 + B_p^2\right)/|B_p|$. We assume here that electron-ion Coulomb collisions act as a breaking force. In this manner, the acceleration period can be derived based on the magnetic field angle at the X-point.

The experimental conditions were $B_t/B_p = 23$, $E_t = 50 \sim 150\mathrm{V/m}$, $n_i = 2\times10^{19}$, $B_p = 0.01\mathrm{mT}$, initial electron temperature $T_e = 10\mathrm{eV}$, and $L = 0.1\mathrm{m}$. Figure 6.3 shows the dependence of the estimated soft X-ray intensity on the effective electric field E_{eff}. Here, the soft X-ray intensity is estimated as $I \propto \int\int T(E) f(E) g_{ff} / v \, dE dv$, where E, $T(E)$, $f(E)$ and g_{ff} are the photon energy, total transmittance (including the absorption effect of rectified aluminum and the Si dead layer, as shown in Fig.5.3), electron velocity distribution function caluclated from the equation of motion and gaunt factor, respectively. Several electrons were accelerated to over 200 eV during their stay inside the reconnection region. The calculation result (Fig. 6.3) shows that the SXR signal appears when E_{eff} exceeds approximately 1000 V/m, which is similar to the experimental results; however, a relatively steeper increasing trend was predicted using the 0D model. Although this calcutlation result show similar trend with the experimental results shown in Fig. 6.2, further investigation is required to understand electron acceralation mechanism.Thus, a new diagnostic to observe the spatial distribution of soft X-ray emission was developed.

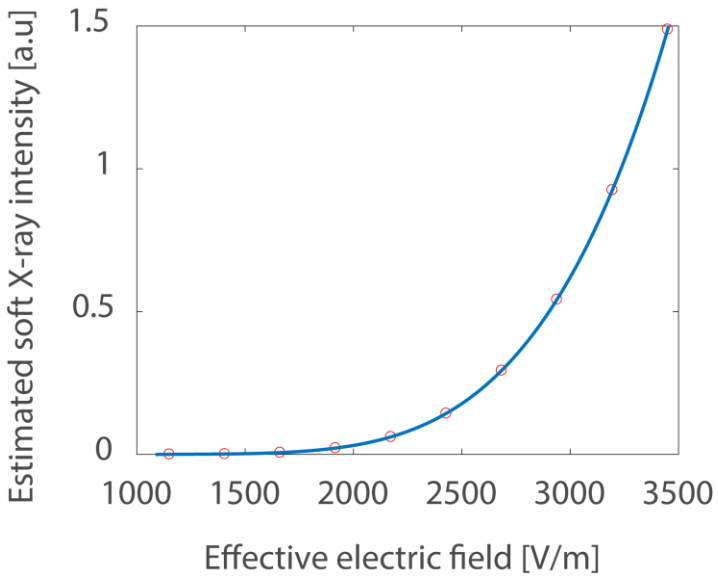

Fig. 6.3. Dependence of estimated soft X-ray intensity, including absorption effect of polycarbonate (2 μm) filter, on E_{eff} .

6.2 Spatial structure of the accelerated electorns near X point

6.2.1 Experimental setup

In the presence of high guide field, efficient electron acceleration along magnetic field line near the X point by reconnection electric field was observed asdescribed in section 6.1. However, the local structure of the soft X-ray emission region was not verified in the experiments. To clarify the spatial structure of the accelerated electrons soft X-ray imaging system was developed (For details, see Chap. 5.). Soft X-ray images were observed by both the look up and the tangential view of the X point region as shown in Fig. 6.4. Visible images converted from incident soft X-ray on phosphor plate were recorded by fast camera SA-Z (Photron). Typical frame rate and exposure time was 210000 frame /sec and 1/316981 sec, respectively. Thin mylar foil (1 μm) was employed on the pinhole to observe the bremsstrahlung caused by tail components of the electron energy distribution function as shown in Fig.5.6.

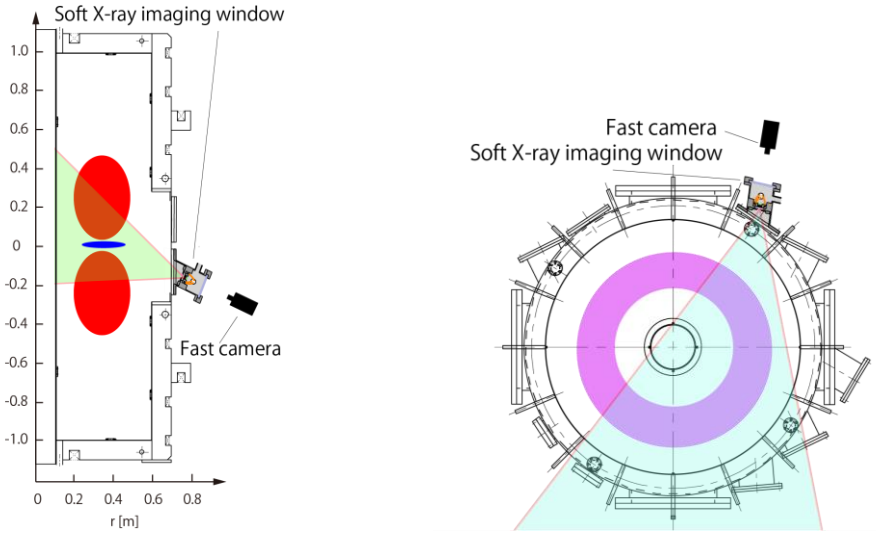

(a) (b)

Fig. 6.4. Two soft X-ray imaging views, (a) look up view and (b) tangential view of the reconnection X point.

6.2.2 Ring shape emission

Figure. 6.5 (a) shows the waveforms of (top) the reconnected magnetic flux, (bottom) the reconnection electric field and (b) shows the poloidal magnetic flux profile and soft X-ray image seen from the look up view. As shown in fig. 6.5 (a), reconnection process proceeded from about t = 9510μsec to 9570μsec. A sharp soft X-ray ring structure located near the X point was observed only in the early phase of magnetic reconnection when the reconnection electric field is high. This local ring shape soft X-ray emission was generated by the high energy tail electrons (>100eV) as shown in fig.5.6. This result suggests that electrons accelerated by reconnection electric field have large toroidal velocity and are localized around the X point region with high toroidal uniformity.

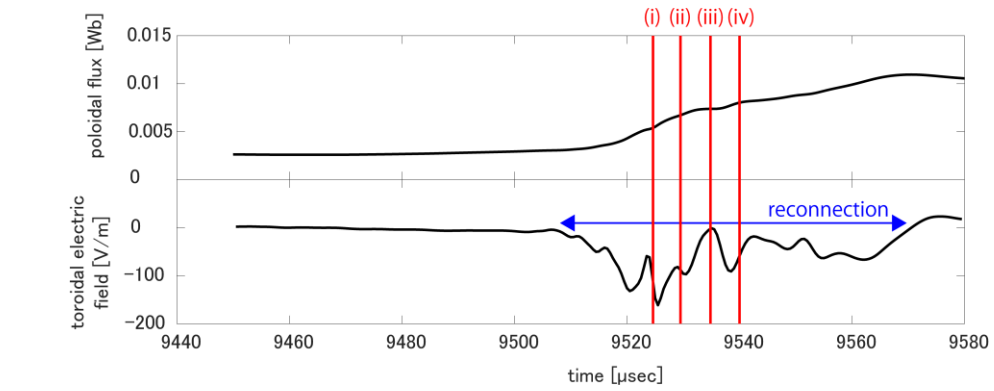

(a)

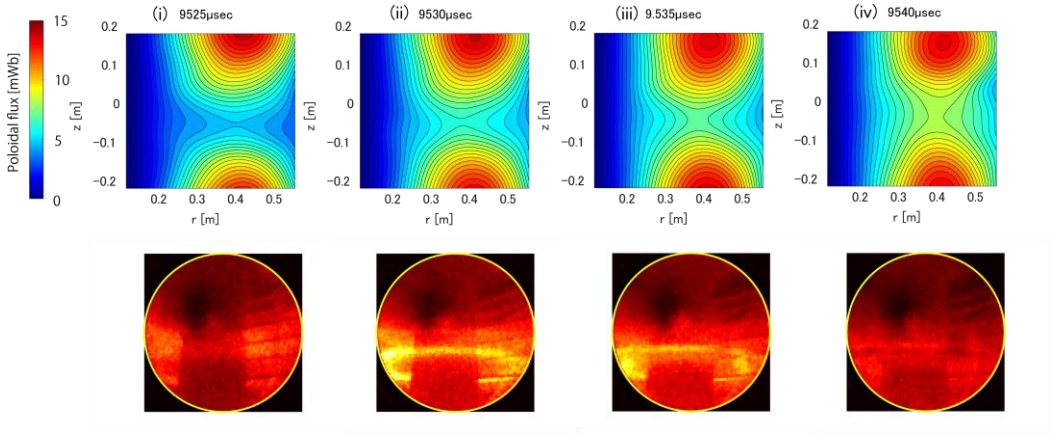

(b)

Fig. 6.5. (a) Evolution of reconnection parameters (top) reconnection magnetic flux and (bottom) toroidal electric field and (b) soft X-ray image (mylar:1μm) during reconnection. Corresponding poloidal flux surfaces are also shown (#170528002).

6.2.3 2D soft X-ray emission structure (Bt: ◉)

The ring-shaped SXR emission region observed from the look-up view indicates that the accelerated electrons distribute uniformly in the toroidal direction. Given the toroidal symmetry, the detailed structure of accelerated electrons can be obrtained by the reconstruction technique applied on the results from the tangential view. Figure.6.6 (a) shows the waveforms of (top) the reconnected magnetic flux, (bottom) the reconnection electric field and (b) shows the poloidal magnetic flux profile and soft X-ray image seen from the tangential view. There were three areas that emit Soft X-ray. Two of them were the upstream ST plasmas st upper and lower regions. The third area was the reconnection region between the two upstresam STs. Since the emission from the reconnection region was observed on nearly horizontal line of sight, local emission reconstruction based on the toroidal symmetry will be avairable. Figure 6.7 shows 2D soft X-ray profile in the vicinity of the reconnection region reconstructed by Abel inversion technique. Soft X-ray emission was mainly observed during the initial phase of magnetic reconnection as well as the results from the look-up view shown in Fig.6.5. First, when electric field slightly ramped up at (i) 9511μsec, relatively wide emission was observed at inboard side of the X point. Secondly, at (ii) 9515.7μsec as reconnection process evolved, the soft X-ray emission was gradually concentrated to the X point region and at (iv) 9520.5μsec then localized near the X point along the two arms of the separatrix. Finally, from (v) 9525.2μsec to (v) 9530μsec the soft X-ray was mainly emitted from the region slightly outward of the X point.

The left-right asymmetric structures of the emissions during mergiing process can simply be explained by the 3D topology of the reconected magnetic field line in high guide field reconnection. When the toroidal field is added on the reconected anti-parallel poloidal field, reconnected magnetic field lines have 3D structure as shown in fig. 2.5. In such a 3D magnetic field line, electrons accelerated at X point can only run on the one side arm of the separatrix. In

Fig. 6.7 (a) these tilted structures agreeed with prediction from the magnetic field structure and the direction of the electron acceleration.

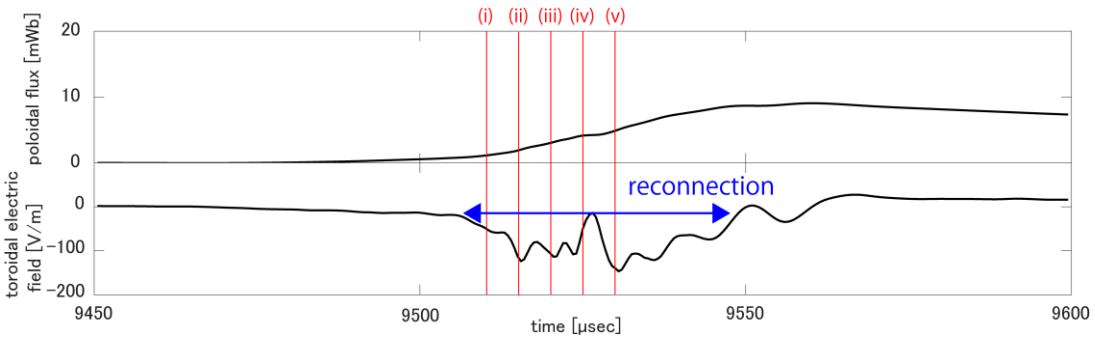

(a)

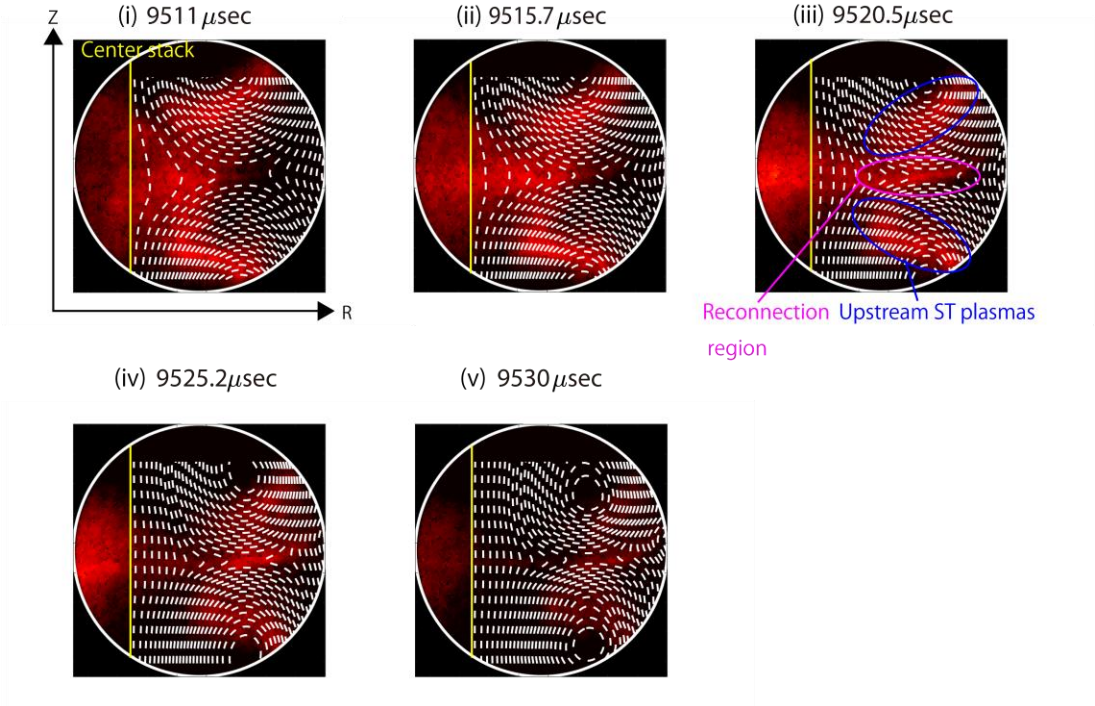

(b)

Fig. 6.6. (a) Evolution of reconnection parameters (top) reconnection magnetic flux and (bottom) toroidal electric field and (b) 2D soft X-ray profile (mylar:1μm) and poloidal flux surfaces in the presence of toroidal magnetic field directed from the surface to the front of the paper (#170524018).

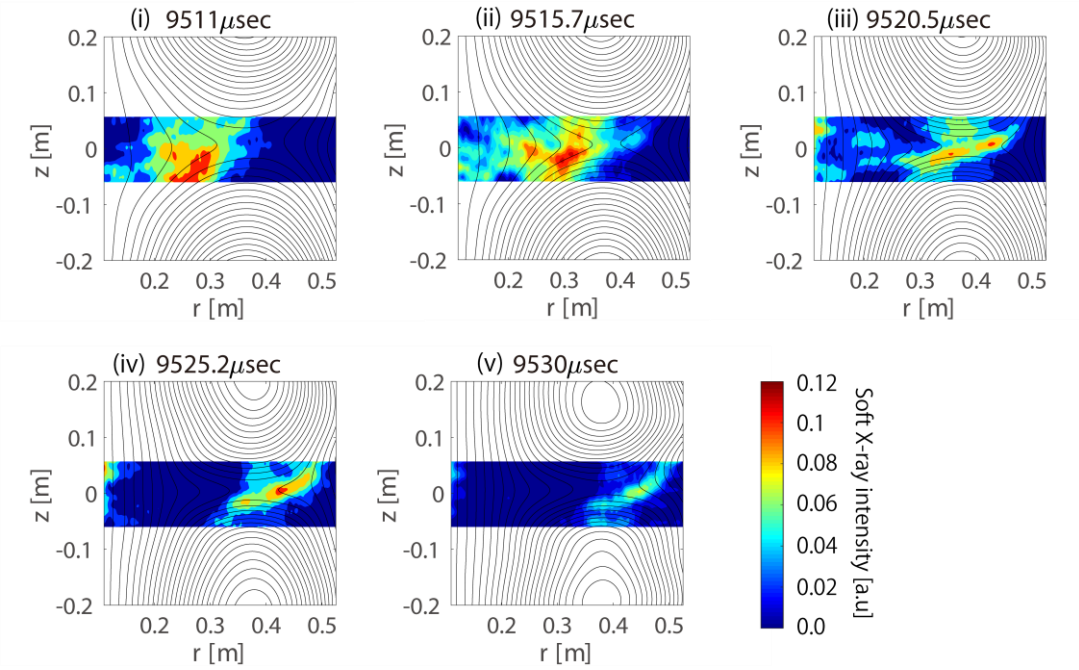

Fig. 6.7. 2D soft X-ray profile (mylar:1μm) reconstructed by Abel inversion directed from the surface to the front of the paper (#170524018).

6.2.4 2D soft X-ray emission structure (Bt: ⊗)

The vertically asymmetric soft X-ray structures showed in section.6.2.2 is thought to be attributed to the spatial structure of accelerated electrons that move along the magnetic field line near the X-point. If so, the soft X-ray structure will be flipped when the reversed toroidal guide field is applied. Therefore, in this section soft X-ray emission structure in the presence of opposite guide field will be shown. The direction of the plasma current was the same as that in section.6.2.2 while the direction of the toroidal field was opposite. Figure 6.8 (a) shows the waveforms of (top) the reconnected magnetic flux, (bottom) the reconnection electric field and (b) shows the poloidal magnetic flux profile and soft X-ray image seen from the tangential view. Figure 6.9 shows 2D

soft X-ray profile reconstructed by Abel inversion technique. Soft X-ray emission was also observed during the initial phase of magnetic reconnection. First, from (i) 9506.2μsec to (iii) 9515.7μsec, the relatively wide soft X-ray emission was observed around upper inboard side of the downstream region. As reconnection process evolved, the soft X-ray emission gradually approached to the X point region from upper inboard side of the downstream. Then soft X-ray emission was localized near the X point along the different pair of the separatrix arm from the case of section.6.2.2. Finally, the soft X-ray was mainly emitted from the region slightly outward of the X point. Thus, in the presence of opposite toroidal field the soft X-ray structures flipped upside down as expected from the electron acceleration process.

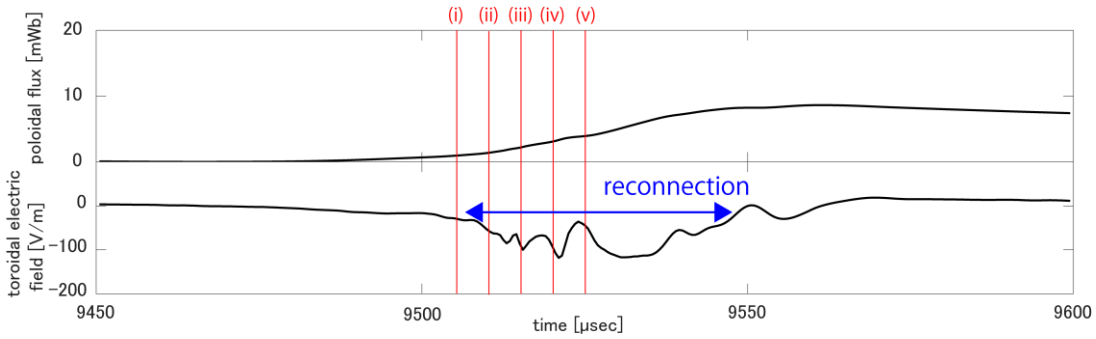

(a)

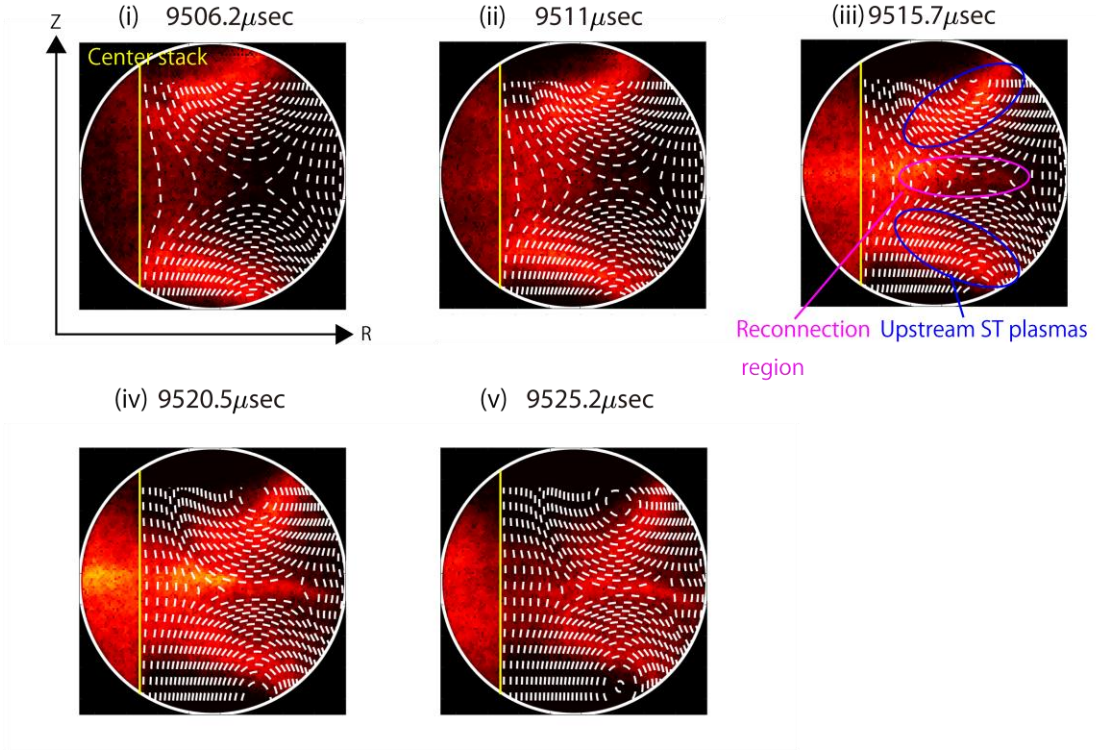

(b)

Fig. 6.8. (a) Evolution of reconnection parameters (t) reconnection magnetic flux and (bottom) toroidal electric field and (b) 2D soft X-ray profile (mylar:1μm) and poloidal flux surfaces in the presence of the toroidal magnetic field directed from the surface to the back of the paper (#170523025).

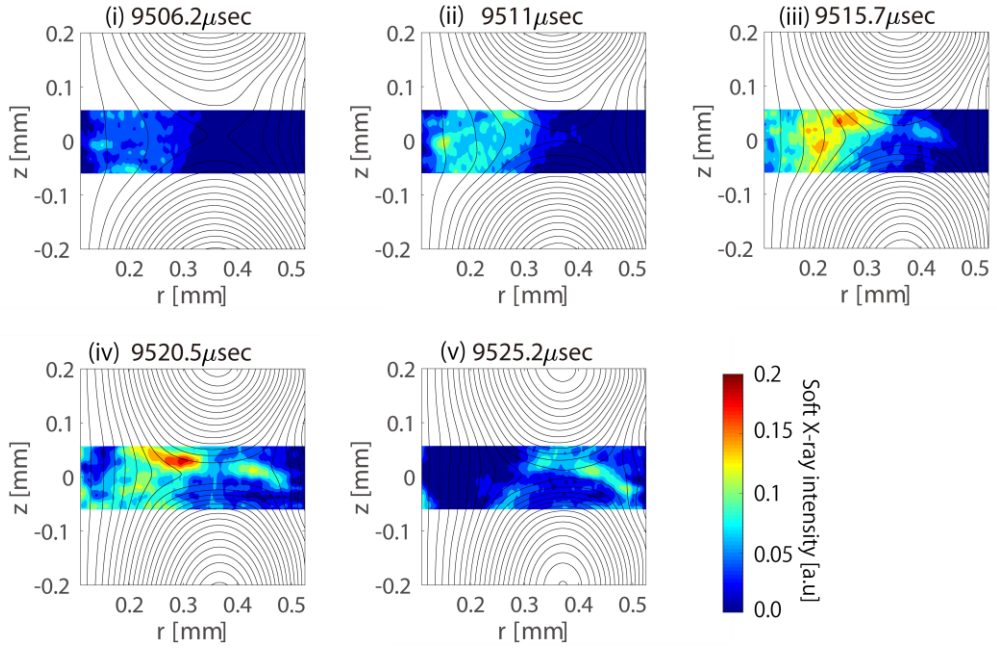

Fig. 6.9. 2D soft X-ray profile (mylar:1μm) reconstructed by Abel inversion directed from the surface to the back of the paper (#170523025).

6.3 Discussion

The left-right asymmetric structures of the accelerated electrons along a pair of the separatrix were reported in section.6.2 and 6.3 as predicted by numerical simulation [35]. However, against all expectations, in the early phase of the merging process relative wide soft X-ray emission region was also observed at inboard side of the downstream region although reconnection electric field was low. In this section, the author will discuss about the possibility whether the electrons can be accelerated by parallel electric field over 100eV at the downstream region in the early phase of the merging process. To verify the experimental results test particle calculation based on the measured magnetic field profile was used. In this calculation I assumed that static electric field on reconnection plane was ignored and parallel electric field was only given by induced electric field in toroidal direction. Electron trajectory was calculated by the equation of motion without collision terrm. Figure.6.10 shows the result of the test particle calculation for the result of Sec.6.2.3. (a) and (b) show the initial test electron locations and the profiles of electron number over 100eV at 9500 and 9520μsec, respectively. 8192 initial electrons were set except in the upstream region as shown in Fig.6.10 (a). The initial electron temperature was set to be 10eV. Typical acceleration time was 4μsec. In Fig.6.10 (b) at 9500μsec electrons are mainly accelerated and get energy over 100eV at downstream region. On the other hand at 9520μsec electrons are mainly accelearted along a pair of the separatrix. These profiles were similar to the measured soft X-ray emisson profiles which suggest the parallel acclereration not only near the X-point but also in the downstream region.

In the presence of the guide field static electric field on the reconnection plane will be generated to suppress the induced parallel electric field except the diffusion region around X point because the charge separation is caused by the different electron and ion flow pattern. However, these

results suggest that in early phase of the merging when the charge separation does not grow to suppress the induced parallel electric field enough, the parallel electric field remained not only inside diffusion region but also in the downstream region and the electrons in the downstream were accelerated by the parallel electric field until the charge separation was established. In the steady reconnection phase, charge separation is enough grown in downstream regions and charged particles move by $E \times B$ drift. In other words, no parallel acceleration is expected in the downstream region. However, experimental results showed wide soft X-ray emission region in the initial reconnection phase. This result suggests that the parallel electric field is not suppressed in the early phase. Test particle cluculation showed similar energetic electron profile when the in-plane electric field was neglected. After that the in-plane electric field was generated and parallel acceleration took place only in the narrow reconnection region.

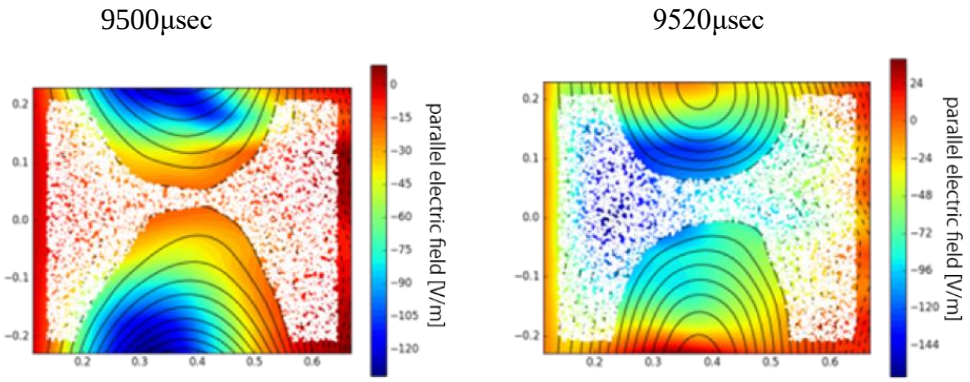

(a)

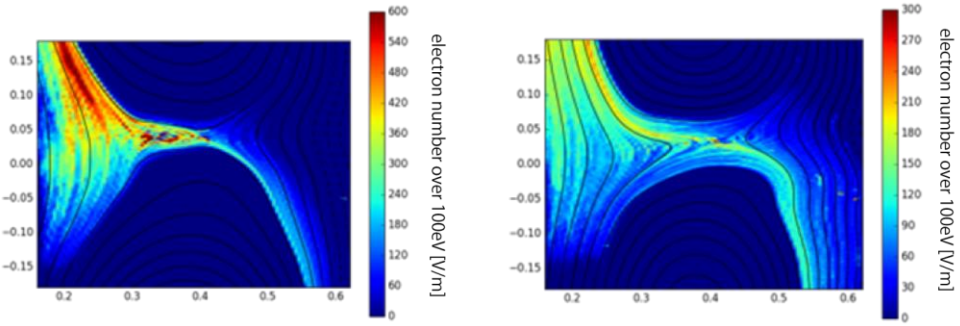

(b)

Fig. 6.10. (a) initial profile of test electrons, (b) electron number profiles (>100eV) at 9505 and 9520μsec, respectively (#170523025).

6.4 Conclusion

To investigate electron energization mechanism during ST merging start-up soft X-ray emission was observed by SBD and soft X-ray imaging system in UTST merging experiments.

Achievement of this research are summarized below.

- Soft X-ray burst over 200eV was observed only during merging and the peak soft X-ray intensity showed positive dependency on the effective electric field around X point. The electron energy over 200eV was consistent with the result of simple 0D model calculation based on electron's duration of stay inside the reconnection region.
- 2D soft X-ray emission profile during merging was observed by soft X-ray imaging system. In very early phase of the merging the relative wide soft X-ray was observed at downstream region and the emission finally formed the left-right asymmetric structure along a pair of the separatrix.
- In test particle calculation, the soft X-ray emisson profile accounted for the parallel acclereration by the induced toroidal electric field. These result suggest that in early phase of the merging when charge separation did not still grow, parallel electric field was induced not only inside diffusion region but also in the downstream region and the electrons in the downstream remarkably were accelerated by the parallel electric field.

Chapter 7

Development of plasma shape reconstruction during spherical tokamak merging

7.1 Issues of plasma shape reconstruction of merging spherical tokamak

In Chap.6 electron energization mechanism during the merging start-up of ST plasma was investigated. However in the present UTST setup the whole electron heating efficiency of merging start-up cannot be evaluated quantitatively partly because the magnetic probe array inside plasma increases the electron loss power as shown in Chap.3. In this Chapter the plasma shape reconstruction of merging ST only based on the magnetic sensors away from plasma was developed. As a difficulty in the ST merging research field, the initial STs in the merging start-up phase do not satisfy the equilibrium condition, however, the magnetic field outside the plasma boundary is defined by Maxwell equations for vacuum condition. Thus the Cauchy Condition Surface (CCS) method [43-50] is effective in the shape reconstruction without introducing any information on the plasma equilibrium. Furthermore, the CCS method is more advantageous from the view point of the reconstruction accuracy than the filament method that represents EFIT [51]. In the filament method, plasma shape and current profile are simultaneously reconstructed dealing with several filament currents inside plasma as unknowns. However, the filament method falls into ill-posed problem because actually there are a number of plasma current profiles to express a specific plasma boundary condition. On the other hand, in the CCS method with the help of

enough magnetic sensors the solution of the plasma shape is uniquely determined without reconstructing plasma current profile because the reconstruction problem of plasma shape and current profile are completely separated as different problem in the CCS method.

Another difficulty that hampers the reconstruction of the merging STs is the influence of the large eddy currents generated on the vessel wall during the merging start-up period, since the initial two STs are formed inductively. These eddy currents should also be correctly evaluated for a reliable reconstruction of magnetic field/flux structure.

Recently, Itagaki et al. proposed an advanced method [50] for the RELAX, a reversed field pinch (RFP) device, where the eddy current effect on the vessel wall is incorporated into the original CCS method algorithm. In more detail, the eddy current term is given by a boundary integral along the vessel in the poloidal direction. The eddy current profile on the vessel is not given in advance but completely unknown before one starts the analysis. That is, the Cauchy conditions and the eddy current values on the vessel nodes are solved simultaneously using only the signals from magnetic sensors. This advanced method t is called “the modified Cauchy condition surface method (the M-CCS method)” , which is considered to be suitable for the reconstruction of the magnetic field structure in the UTST, especially in the ST merging start-up period.

7.2 Modified Cauchy condition surface (CCS) method

To reconstruct merging ST the M-CCS method was adopted. Schematic of this method is shown in Fig.7.1. The CCS and the vacuum vessel boundary are located to describe the plasma current effect and the toroidal eddy current, respectively. Then this is an 'inverse problem' that aims to infer the Dirichlet and the Neumann conditions on the CCS as well as the toroidal current on the vacuum vessel, based on the observation of the magnetic sensor signals outside the plasma. Three types of boundary integral equations to be solved are described as shown below [50].

(a) For poloidal flux sensors at points i

$$\psi_i - W_i^{\psi} = \int_{\Gamma_{CCS}} \left(\frac{\psi^*}{r}\frac{\partial \psi}{\partial n} - \frac{\psi}{r}\frac{\partial \psi^*}{\partial n} \right) d\Gamma + \mu_0 \int_{\Gamma_{VV}} j_{VV}(\mathbf{r}_{VV}) \psi^*(\mathbf{r}_{VV} \to \mathbf{r}_i) d\Gamma(\mathbf{r}_{VV}) \tag{7.1}$$

(b) For magnetic field sensors at points i

$$B_i - W_i^{B} = \int_{\Gamma_{CCS}} \left(\frac{B^*}{r}\frac{\partial \psi}{\partial n} - \frac{\psi}{r}\frac{\partial B^*}{\partial n} \right) d\Gamma + \mu_0 \int_{\Gamma_{VV}} j_{VV}(\mathbf{r}_{VV}) B^*(\mathbf{r}_{VV} \to \mathbf{r}_i) d\Gamma(\mathbf{r}_{VV}) \tag{7.2}$$

(c) For points i on the CCS

$$-W_i^{CCS} + c_i \psi_i = \int_{\Gamma_{CCS}} \left(\frac{\psi^*}{r}\frac{\partial \psi}{\partial n} - \frac{\psi}{r}\frac{\partial \psi^*}{\partial n} \right) d\Gamma + \mu_0 \int_{\Gamma_{VV}} j_{VV}(\mathbf{r}_{VV}) \psi^*(\mathbf{r}_{VV} \to \mathbf{r}_i) d\Gamma(\mathbf{r}_{VV}) \tag{7.3}$$

where ψ means the magnetic flux function [Wb/rad], and c_i is a constant that depends on the local boundary geometry on the CCS [24]. In Eqs. (7.1)-(7.3), W_i^{ψ}, W_i^{B} and W_i^{CCS} are the contributions of the external coil current to the point i. In each equation, ψ^* is the fundamental solution which satisfies the equation

$$-\left\{ r\frac{\partial}{\partial r}\left(\frac{1}{r}\frac{\partial}{\partial r} \right) + \frac{\partial^2}{\partial z^2} \right\} \psi^* = r\delta(r-a)\delta(z-b), \tag{7.4}$$

where $\delta(r-a)$ and $\delta(z-b)$ are Dirac's delta function. Equation (7.4) describes the axisymmetric poloidal flux function for an arbitrary field point (r,z) caused by a toroidal current spike at the coordinate (a,b). Then the fundamental solution ψ^* is given by

$$\psi^* = \frac{\sqrt{ar}}{\pi k}\left[\left(1 - \frac{k^2}{2} \right) K(k) - E(k) \right], \tag{7.5}$$

with

$$k^2 = \frac{4ar}{(r+a)^2 + (z-b)^2}, \tag{7.6}$$

where $K(k)$ and $E(k)$ are the complete elliptic integrals of the first and the second kind, respectively. The quantity $B^*(\mathbf{r}_{VV} \to \mathbf{r}_i)$ means $B^* = -\mathbf{n_0} \cdot \nabla \psi^* / r$ with $\mathbf{n_0}$ being the assigned vector normal to the direction of the 'magnetic probe' located at the point i. The quantity $\mathbf{r}_{VV}$ denotes an arbitrary point on the vacuum vessel. $j_{VV}(\mathbf{r}_{VV})$ shows the linear density [A/m] of the toroidal eddy current on the vacuum vessel.

In each of Eqs. (7.1)-(7.3) the first term on the RHS comes from the original CCS method formulation. These parts of the boundary equations are derived from the Grad-Shafranov equation for a vacuum field [52]. The second term on the RHS of each Eqs. (7.1)-(7.3) describes the contribution of the eddy current. Once both of the boundary conditions on the CCS and the current density profile on the vacuum vessel have been solved, the magnetic flux value can be calculated at an arbitrary point outside the plasma.

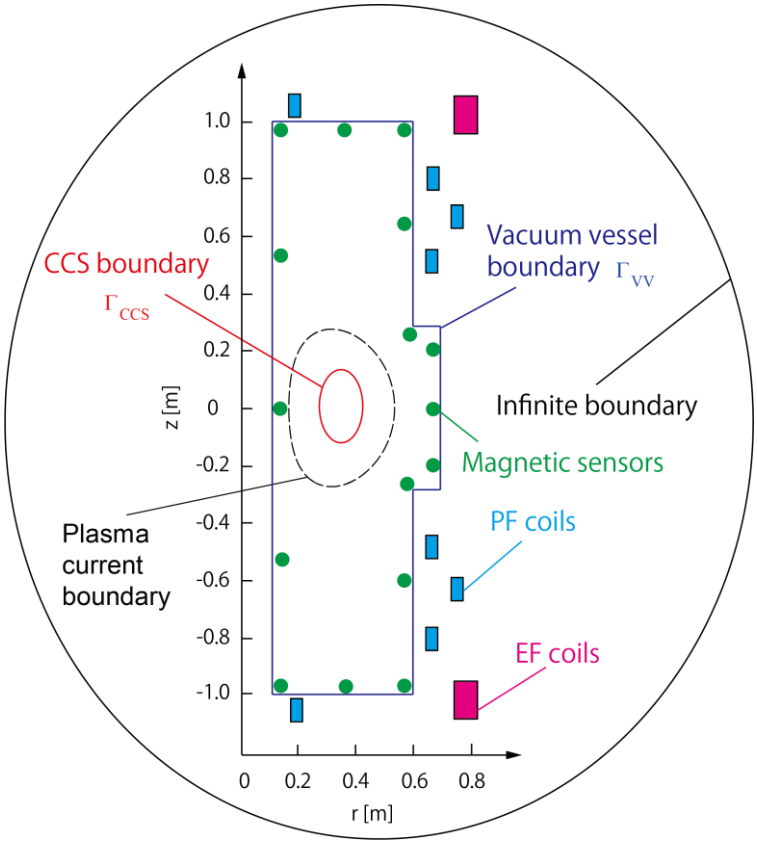

Fig. 7.1. Schematic of modified CCS method.

7.2.1 Boundary elements for descretization

The CCS and the vacuum vessel boundary are discretized using a set of discontinuous quadratic boundary elements. Illustration of discontinuous quadratic boundary elements is shown in Fig. 7. 2. A boundary element consists of mesh points and nodes. The mesh points define the shape of boundary element, while the nodes are points to give the physical quantities. Now a local coordinate ξ is introduced which ranges from -1 to 1. Then the geometry coordinate (r,z) on a boundary element is given by

$$r = \phi_1 r_1 + \phi_2 r_2 + \phi_3 r_3, \quad z = \phi_1 z_1 + \phi_2 z_2 + \phi_3 z_3 \tag{7.7}$$

with the interpolation functions

$$\phi_1 = \xi(\xi - 1)/2, \quad \phi_2 = (1-\xi)(1+\xi) \quad \text{and} \quad \phi_3 = \xi(1+\xi)/2. \tag{7.8}$$

This quadratic element is convenient for arbitrary geometries and provides good approximation of physical quantities. The physical quantities ψ, $\partial\psi/\partial n$ and the eddy current j are interpolated as

$$\psi(\zeta) = \Phi_1(\zeta)\psi_1 + \Phi_2(\zeta)\psi_2 + \Phi_3(\zeta)\psi_3, \tag{7.9}$$

$$\frac{\partial\psi}{\partial n}(\zeta) = \Phi_1(\zeta)\left(\frac{\partial\psi}{\partial n}\right)_1 + \Phi_2(\zeta)\left(\frac{\partial\psi}{\partial n}\right)_2 + \Phi_3(\zeta)\left(\frac{\partial\psi}{\partial n}\right)_3, \tag{7.10}$$

$$\text{and} \quad j(\zeta) = \Phi_1(\zeta) j_1 + \Phi_2(\zeta) j_2 + \Phi_3(\zeta) j_3. \tag{7.11}$$

Here, the interpolation functions for the physical quantities are different from the shape functions of Eq. (7.8), since the node points at both ends are shifted toward the inside. This type of boundary element is called the discontinuous element or the non-conforming element, as the physical quantities are not assumed to be continuous at both ends of an element. The interpolation functions adopted here have the forms

$$\Phi_1(\zeta) = \frac{3}{4}\zeta\left(\frac{3}{2}\zeta - 1\right), \Phi_2(\zeta) = \left(1 - \frac{3}{2}\zeta\right)\left(1 + \frac{3}{2}\zeta\right) \quad \text{and} \quad \Phi_3(\zeta) = \frac{3}{4}\zeta\left(\frac{3}{2}\zeta + 1\right). \tag{7.12}$$

This use of the discontinuous elements is highly important to avoid the so-called "corner point" problem. If one uses ordinary continuous elements, a corner point sandwiched between two elements has two different values for the normal derivative of magnetic flux function depending on the side under consideration, as two continuous boundary elements hold one nodal point in common. To avoid this trouble, the adoption of the discontinuous elements is strongly recommended, especially for the D-shaped CCS that has two corner points (later shown in Fig.7.5(c)).

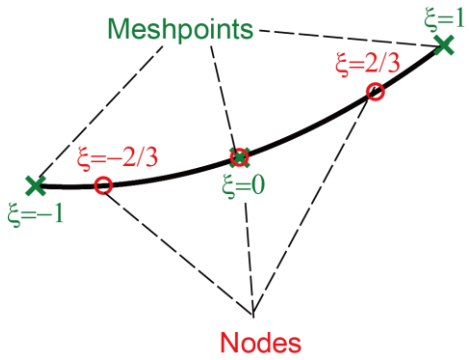

Fig. 7.2. Illustration of the discontinuous quadratic boundary element

7.2.2 Regularization technique

In this way, finally, Eqs. (7.1)-(7.3) are discretized, coupled and can be expressed in a matrix equation form

$$\mathbf{Dp} = \mathbf{g}\,. \tag{7.13}$$

The matrix equation (7.13) is solved using the singular value decomposition (SVD) technique

[53] in such a way that the least square norm $||\mathbf{Dp}=\mathbf{g}||$ is minimized. The matrix $\mathbf{D}$ is decomposed as $\mathbf{D}=\mathbf{U}\Lambda\mathbf{V}^{\mathrm{T}}$, where $\mathbf{U}$ and $\mathbf{V}^{\mathrm{T}}$ are orthogonal matrices and Λ is a diagonal matrix with positive singular values or zero components. The solution in this case is given by

$$\mathbf{p}=\mathbf{V}\Lambda^{-1}\mathbf{U}^{\mathrm{T}}\mathbf{g}. \tag{7.14}$$

To cut out high frequency modes and avoid a numerical instability of the solution, the so-called truncated singular value decomposition (TSVD) technique [53] is used. In this technique, the regularized solution is given by

$$\mathbf{p}_k=\mathbf{V}\Lambda_k^{-1}\mathbf{U}^{\mathrm{T}}\mathbf{g}. \tag{7.15}$$

Here Λ_k means that the singular values smaller than the component λ_k in Λ are omitted so that the condition number [53] is not larger than a certain value.

7.3 Reconstruction for UTST device (test calculation)

7.3.1 Analytical setting

Three representative phases (a. initial phase, b. merging phase, c. after merging) are considered to model limiter configurations in the UTST device, as a typical example of a spherical tokamak merging start-up. The vacuum vessel is regarded as axisymmetric in the toroidal direction and its cross section has a convex shape as shown in FIG. 7.1. The reference distributions of magnetic flux and the eddy current on the vacuum vessel were analyzed beforehand using a UTST equilibrium code. Figures 7.3 (a)-(c) show the reference poloidal flux profiles in these three phases. The blue heavy lines and red points show the plasma boundaries and limiter-plasma contact positions, respectively. In the following discussion, only the equilibrium field (EF) coil current effect is considered as the external coil effect in the formations of the flux distribution.

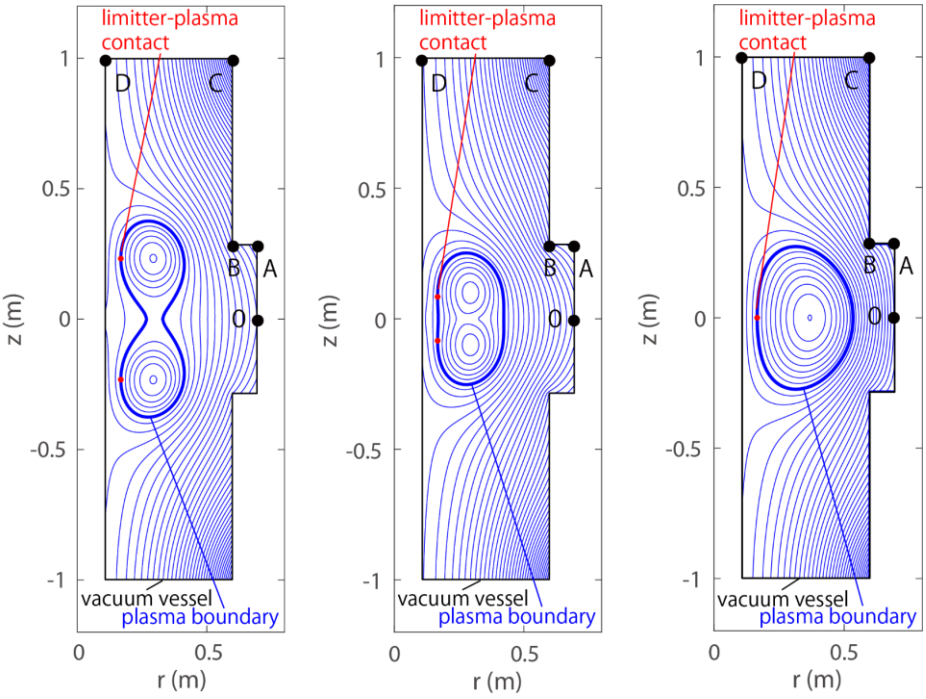

(a) initial phase (b) merging phase (c) after merging

Fig. 7.3 Reference poloidal flux profile in merging initial phase, merging phase and after merging

7.3.2 Location of sensors and analytic nodes

The magnetic sensor signals were also generated from the reference flux profiles. The sensor locations in this test calculations are illustrated in Fig. 7.4 (a). One assumes 47 flux loops and 43 field sensors, i.e., a total of 90 magnetic sensors inside the vacuum vessel. The field sensors detect the poloidal magnetic field in a certain direction.

Segmentation of the conductor wall is shown in Fig. 7.4 (b). The convex shape of vacuum vessel is divided into 17 discontinuous quadratic boundary elements, so that the total number of nodes is 51 and the number of unknowns on vacuum vessel is 51. Further, the CCS shapes are set differently in each merging phase. The CCS segmentations in the three phases are shown in Fig. 7. 5. The numbers of CCSs, boundary elements and nodes are listed in Table 7.1. In each of a.

initial phase and b. merging phase two separated CCSs are set to enclose the corresponding two magnetic axes. In c. after merging, one sets a “D-shaped” CCS that is supposed to be almost similar to the shape of LCFS. When this method is applied for real time control of merging ST, the number of CCSs has to be changed from two to one at a certain point of time. In each phase, a total of 6 discontinuous quadratic boundary elements are used, so that the numbers of nodes and unknowns on the CCS are 18 and 36, respectively. Eventually, the total number of unknowns is 87, which is smaller than a total of 90 magnetic sensors. Then the uniqueness of the solution is guaranteed.

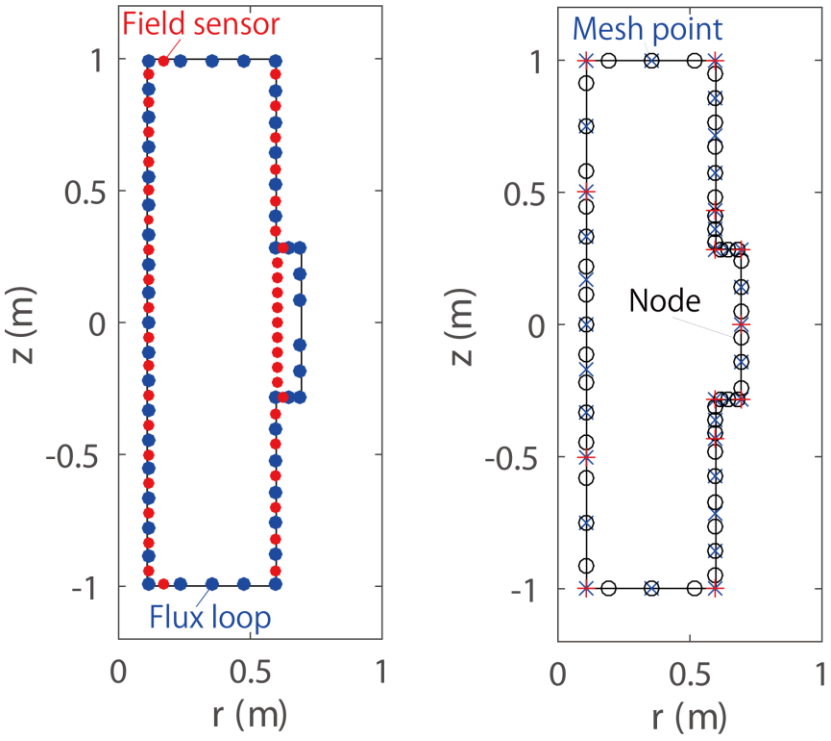

(a) sensor locations (b) segmentation of the vacuum vessel wall

Fig. 7.4 Sensor locations and segmentation of the vacuum vessel wall

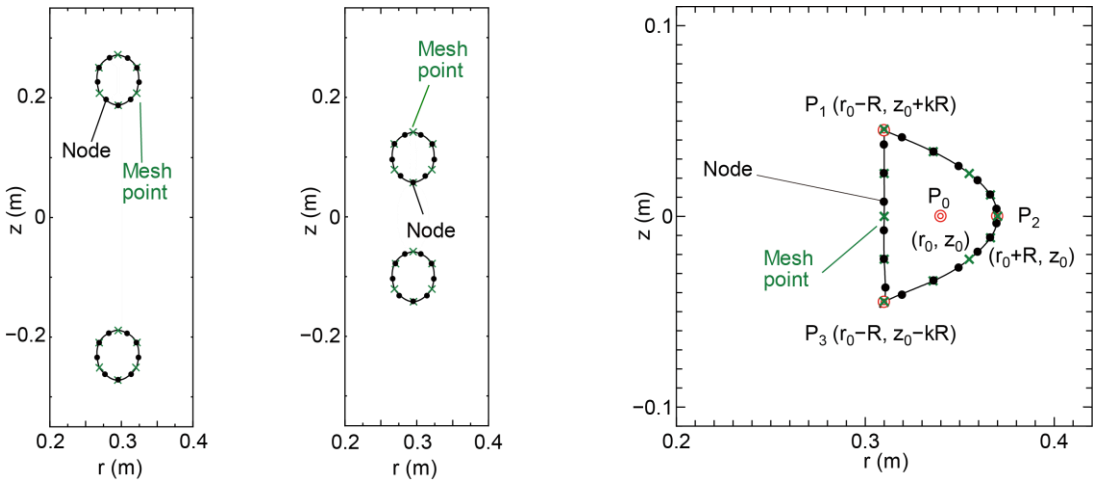

(a) initial phase (b) merging phase (c) after merging

Fig. 7.5 CCS segmentations at initial phase, merging phase and after merging

phase	No. of CCSs	No. of boundary elements	No. of nodes
(a) initial phase	2	3×2	18
(b) merging phase	2	3×2	18
(c) after merging	1	6	18

Table. 7.1. The numbers of CCSs, boundary elements and nodes in each phase

7.3.3 Reconstructed poloidal flux profile and plasma boundary shape

The magnetic flux distributions and the eddy current profile were reconstructed in three different phases and the influence of sensor signal noise was studied. The Gaussian noises were numerically added to magnetic sensor signals. In the present study, one added a noise with 3 % standard deviation to each sensor signal. Figures 7. 6 (a), (b) and (c) show the reconstructed flux profiles in the three different phases. In each figure the magenta dashed contours show the reference solution, while the black solid contours indicate the reconstructed solution (noise: 0 %).

The blue, red, green solid lines show the reference plasma boundary, the reconstructed plasma boundary (noise: 0 %) and the reconstructed plasma boundary (noise: 3 %), respectively. Further, the reconstructed poloidal magnetic field profile in each phase was shown in Fig. 7. 7. In each figure, the abscissa denotes the distance from the "start" point that is indicated in each corresponding figure in Fig. 7. 6, in the counterclockwise direction along the perimeter of the reference plasma boundary. The blue, red and green solid lines show the reference poloidal magnetic field profile, the reconstructed poloidal magnetic field profile (noise: 0 %) and the reconstructed poloidal magnetic field profile (noise: 3 %) on each plasma boundary, respectively. Table 7.2 shows the number of singular values that are not truncated, the reference and the reconstructed total plasma current (Ip) in each calculation. The reconstructed Ip was calculated based on the following equation using the reconstructed plasma boundary condition

$$I_{\mathrm{p}} = \frac{1}{\mu_0}\int_{\Gamma_{\mathrm{p}}}\left(\frac{1}{r}\frac{\partial \psi}{\partial n}\right)d\Gamma \,. \tag{7.16}$$

As shown in Fig. 7. 6, the reconstructed flux profile in each case shows a good agreement with the reference profile except in the vicinity of $z = 0$ in Phase a (initial phase). In Phase a, the two separated plasma boundaries are shown in the reconstruction, while the reference plasma has a single boundary. However, in $|z| \geq 0.1\,\mathrm{m}$, when the sensor noise was not added, the discrepancy of the reconstructed plasma boundary from the reference plasma boundary (in the direction normal to the reference boundary) was less than 6 mm in Phase a (initial phase). With 3 % noise, the discrepancy in Phase a was less than 25 mm in $|z| \geq 0.1\,\mathrm{m}$.

On the other hand, in each of Phases b (merging phase) and c (after merging), the reconstructed plasma has a single boundary as the same as the reference one. When the sensor noise was not added, the discrepancy was less than 5 mm in Phase b and less than 3 mm in Phase c. When considering the sensor signal noise, the discrepancy increases as a natural result. With 3 % noise, the discrepancy was less than 11 mm in Phase b and less than 6 mm in Phase c.

The slightly large plasma boundary discrepancy in the vicinity of $z = 0$ in Phase a is thought to be caused by the reference magnetic configuration itself. The plasma boundary discrepancy Δr along the line $z = 0$ can be estimated to be

$$\Delta r = \left(\frac{\partial \psi}{\partial r} \right)^{-1} \Delta \psi \ . \tag{7.17}$$

That is, the plasma boundary discrepancy Δr caused by the poloidal flux error $\Delta \psi$ increases in the region where the gradient of the poloidal flux is small. This trend causes large boundary discrepancy in the vicinity of $z = 0$, however, this estimation error may not degrade the performance of the M-CCS method for the purpose to evaluate the plasma position and the current.

The poloidal magnetic field profile on the plasma boundary was reconstructed accurately in each phase, as shown in Fig. 7.7. Further, tabele 7.2 shows that the reference error of total Ip was smaller than 0.08 %, 1.2 % and 0.12 % respectively in Phase a, b and c even if the 3 % noise was added.

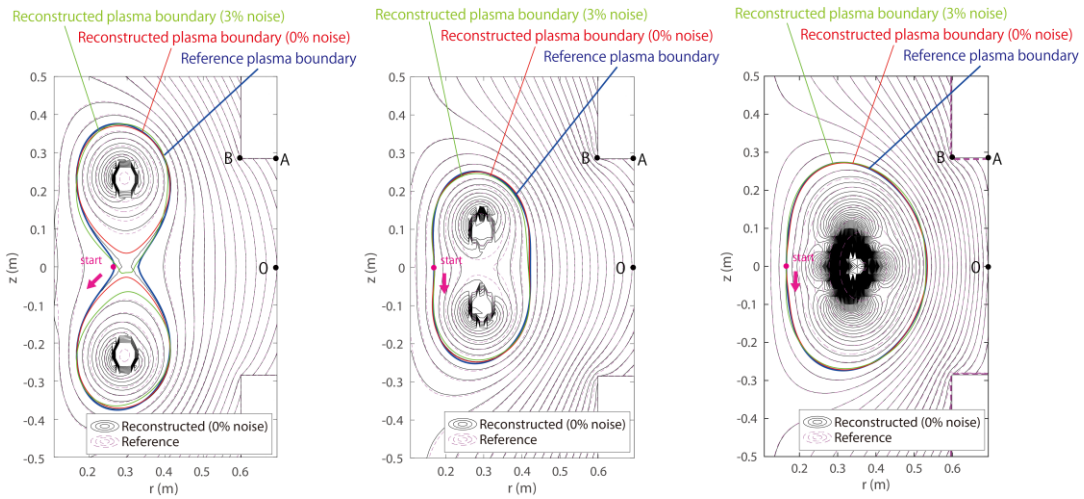

(a) initial phase (b) merging phase (c) after merging

Fig. 7.6 The reconstructed poloidal flux profiles at initial phase, merging phase and after merging

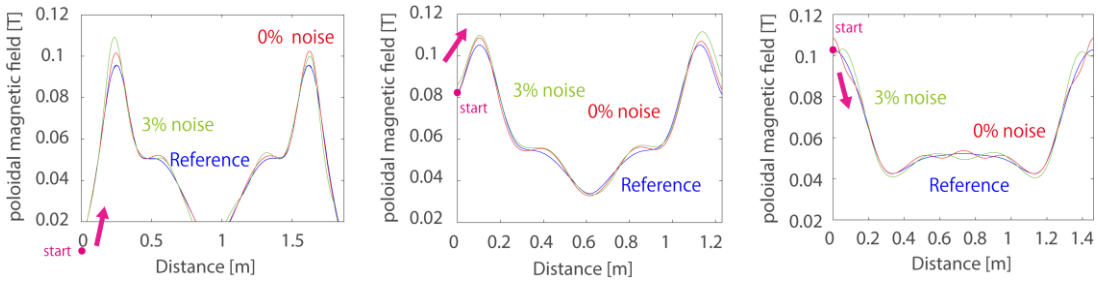

(a) initial phase (b) merging phase (c) after merging

Fig. 7.7 The reconstructed poloidal magnetic field profiles along the plasma boundary at initial phase, merging phase and after merging (The abscissa denotes the distance (journey) along the perimeter of the reference plasma boundary.)

Phase	Added sensor noise (%)	No. of not truncated singular values	Reference Ip (kA)	Reconstructed Ip (kA)
(a) initial phase	0	77	70.00	70.23
	3	76		70.52
(b) merging phase	0	74	66.41	66.77
	3	72		67.20
(c) after merging	0	80	70.00	70.12
	3	76		70.81

Table 7.2. The truncated number of singular values, reference and reconstructed total plasma current in each phase

7.3.4 Reconstructed eddy current profile

The reconstructed eddy current profiles in the three phases are shown in FIG. 7. 8. The blue, red, green solid lines show the reference eddy current profiles, the reconstructed eddy current profiles (noise: 0 %) and the reconstructed eddy current profiles (noise: 3 %), respectively. In the present study a thin wall approximation was assumed, so that the unit of eddy current density is described as [MA/m]. Symbols of A, B C and D in FIG. 7. 8 show the positions on the vacuum vessel that are previously indicated in FIG. 7. 3. In each phase, when the noise was not added, the eddy current profile on vacuum vessel was reconstructed with fairly good accuracy. When the 3 % noise was added, the reconstructed eddy current profiles became inaccurate, however the results roughly reproduce the whole profiles.

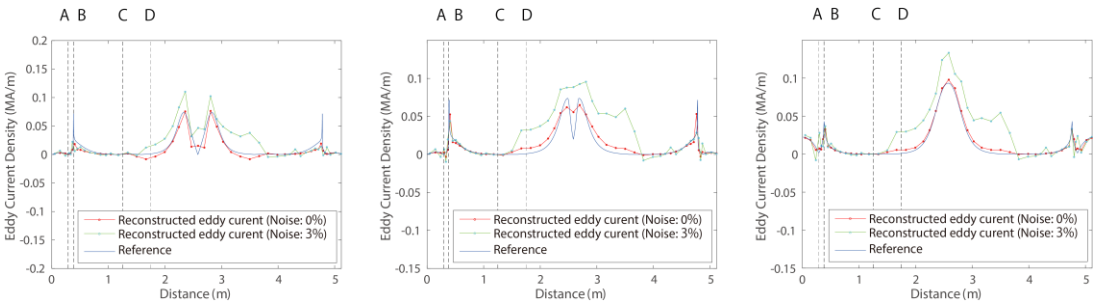

(a) initial phase (b) merging phase (c) after merging

Fig. 7.8 The reconstructed eddy current profiles on the vacuum vessel at initial phase, merging phase and after merging (The abscissa denotes the distance (journey) along the perimeter of the vacuum vessel boundary. Symbols A, B, C, and D show the positions of the vacuum vessel corners that are indicated in Fig. 7. 3.)

7.4 Possibility of introduction of Hansen's L curve method

The aim of the present research is to seek the best analytic conditions for the reconstruction by comparing the reconstructed solution with the reference solution that was given directly using a MHD equilibrium code. That is, the author sought the optimized number of cut-off singular values in such a way that the reconstructed profiles agree well with the reference solutions. However, it's necessary to decide automatically the optimized number of cut-off singular values. In this section the capability of Hansen's L-curve method [54] was investigated.

The present boundary integral formulation is discretized and finally converted to a form of matrix equation $Ax = b$, where x is the vector of reconstructed solution that depends on the number of cut-off singular values, while b denotes the vector containing the known sensor

signals. Hansen's L-curve method is based on the plot of the solution norm $\|x\|^2$ vs. the residual norm $\|Ax-b\|^2$ (as a function of number of cut-off singular values in the present case). The plot usually represents an L-shaped curve, and it can be supposed that the corner or the flex point of the L-curve suggests the optimal number of cut-off singular points. Figures 7. 9 (a) – (c) show the L-curves for cases we deal with. Even if the 3% noise was added, these cases clearly show L-curves, and in each of these cases the flex point closely indicates the number of singular values we adopted.

These calculation don't spend much calculation cost because $\|x\|^2$ and $\|Ax-b\|^2$ can easily be got. So it is very convenient to decide the optimized number of cut-off singular values. In the following section, the number of cut-off singular values will be decided by the L curve method.

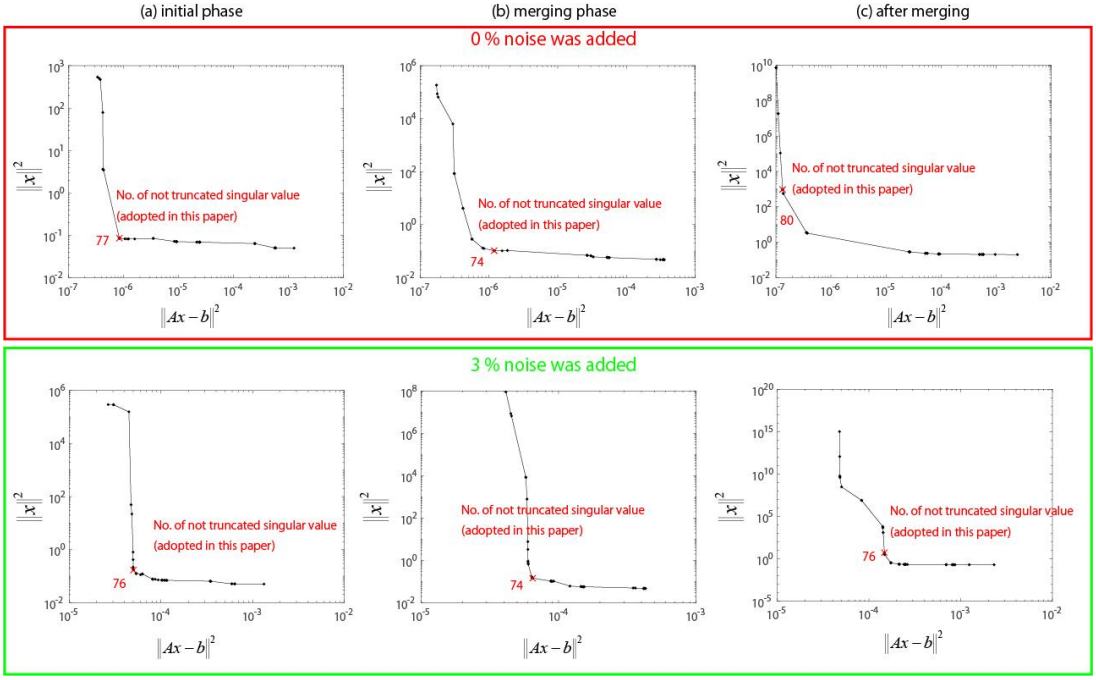

Fig. 7.9 Hansen's L curve

7.5 Reconstruction for ST40 (test calculation)

7.5.1 Analytical setting

In this section, merging compression operation (For details, see Chap. 1.) for ST40 was considered. The reference distributions of magnetic flux and the eddy current on the vacuum vessel were analyzed beforehand using fiesta and RZIP code [24] which has been used for modeling merging compression start-up scenario in ST40.

The reference flux profiles in UTST employed in sections 7.2-4 was obtained under the assumptions that the time constant of external coil currents were much longer than the resistive time of the wall and that of plasma current was much shorter. Thus the time evolutions of the coil/plasma/eddy currents were not taken into account. On the other hand, the references for ST40 were the snapshots of the evolving flux surfaces calculated by fiesta and RZIP code considering the self inductances of the plasmas and mutual inductances between plasma and conductor walls. Figure. 7. 10 shows coils, passive and plasma current waveforms simulated by fiesta + RZIP code for merging compression start-up of ST40. In the present study three references at representative timing, 360, 364, 368msec were used. Figure. 7. 11 (a), (b) and (c) show poloidal flux profile at each timing. In this analysis the in-vessel coil (Merging Compression coil) current is also known because MC coil current can be measured by Rogowski coil experimentally.

7.5.2 Location of sensors and analytic nodes

The magnetic sensor signals were also given from the reference flux profiles. The sensor locations which were utilized for reconstruction in ST40 are illustrated in FIG. 7.12 (a). 46 flux loops and 34 field sensors, a total of 80 magnetic sensors around the device were utilized. The

field sensors detect the poloidal magnetic field in a certain direction. The part of flux loops are in outside of the inner vacuum vessel.

Segmentation of the conductor wall is shown in FIG. 7.12 (b). As shown in FIG. 7.12 (b), actual device has some other conductor components, such as coil shields, cryostat, etc, in addition to the vacuum vessel wall. To consider the eddy currents induced on these additional conductor components the reconstruction code was improved so that for calculating eddy current effect correctly several sets of boundary can be located for calculating eddy current effect correctly regardless of whether the assumed boundary is closed or not though in the conventional code only a close vacuum vessel boundary can be described. The flux loops which locate outside of the inner vacuum vessel can hereby be utilized for reconstruction. In ST40 case, these boundaries are divided into 38 normal quadratic boundary elements to reduce unknowns of the eddy currents, so that the total number of nodes is 78 and the number of unknowns on conductor components is 78.

Further, the CCS shapes are set differently in each time as well as the UTST analysis. The CCS segmentations in the each time are shown in FIG. 7. 13. The numbers of CCSs, boundary elements and nodes are listed in TABLE. 7.3. In merging phase, at t=360, 364msec two separated CCSs are set to enclose the corresponding two magnetic axes. At t=368msec, one sets a “D-shaped” CCS. Then boundary elements should densely be set in outboard region of the D-shape for accurate reconstruction. This necessity of setting boundary elements densely in outboard region is appeared to help the small number of sensors in the outboard region of ST40 device as shown in fig. 7.12 (a). In each phase, a total of 6 discontinuous quadratic boundary elements are also used, so that the numbers of nodes and unknowns on the CCS are 18 and 36, respectively. Eventually, the total number of unknowns is 114, which is unfortunately larger than a total number of 80 magnetic sensors. Then the uniqueness of the solution is not guaranteed. However, in ST40, analysis setting with large number of boundaries as accurately as possible to model conductor

components is clearly better than the setting with small number of boundaries which satisfies that the number of unknowns is smaller than the sensor numbers. It seem to be reasonable because regularization method are used in this method.

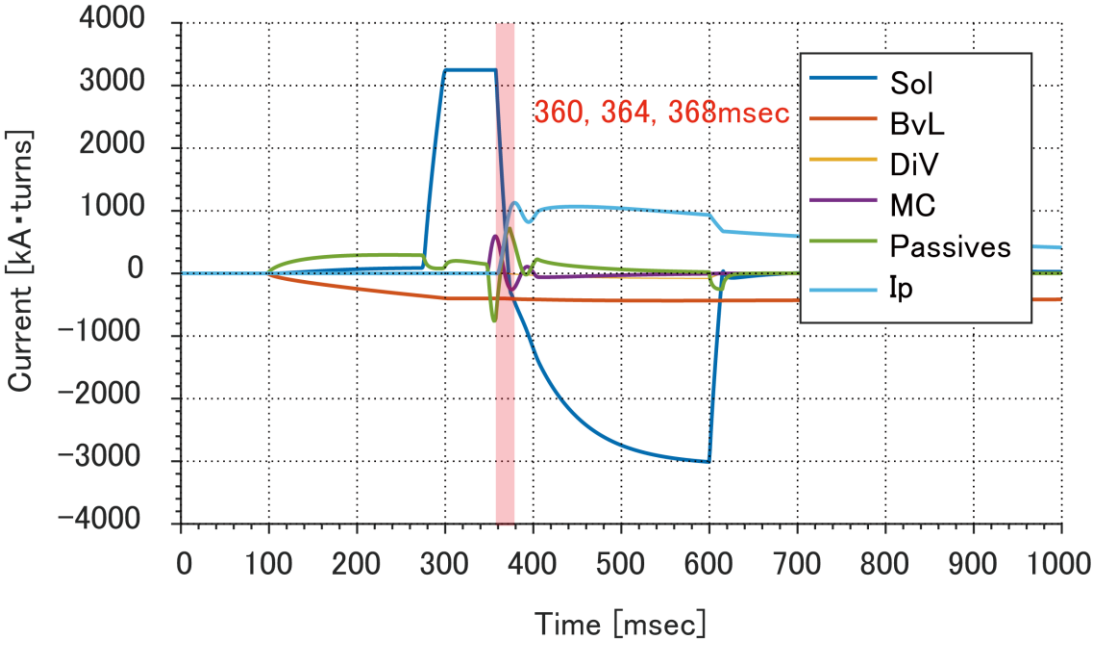

Fig. 7.10 Coils, passive and plasma current waveforms simulated by fiesta + RZIP code for merging compression start-up of ST40 (Courtesy of S. McNamara (Tokamak Energy L.t.d.))

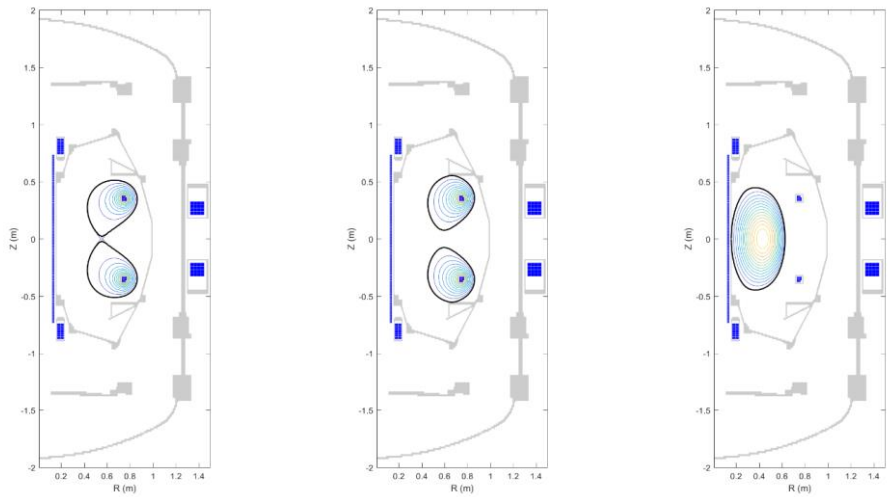

(a) (b) (c)

Fig. 7.11 poloidal flux profile at (a) 360msec, (b) 364msec and (c) 368msec (Courtesy of S. McNamara (Tokamak Energy L.t.d.)).

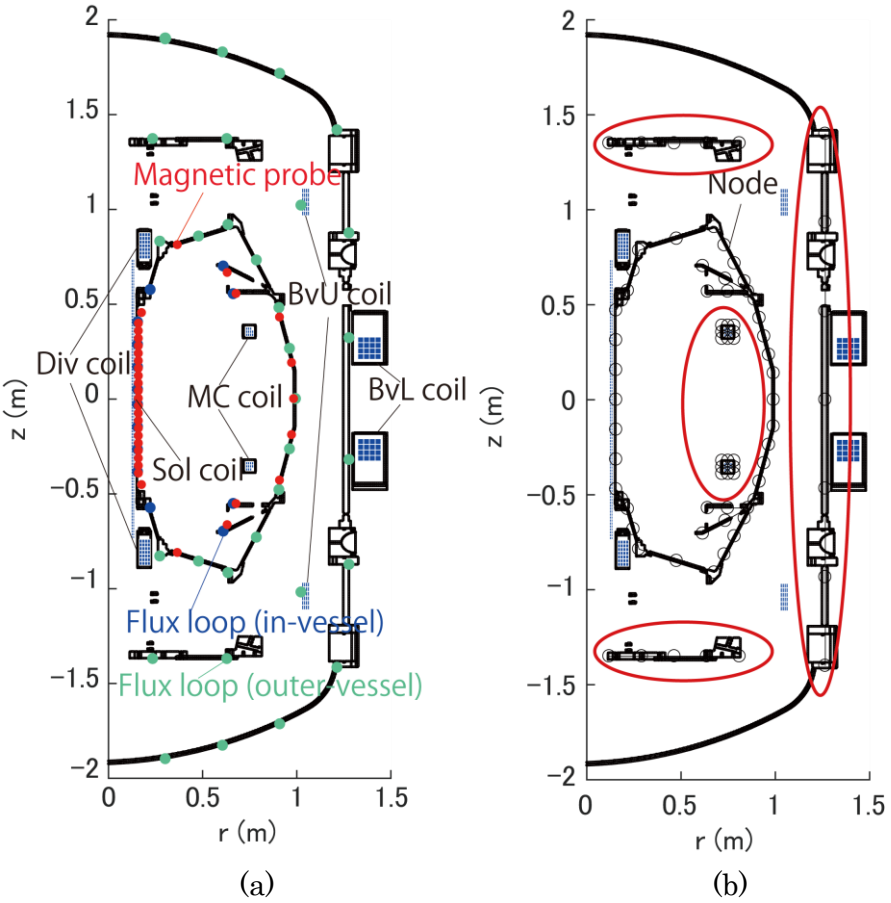

Fig. 7.12 (a) The sensor locations which were utilized for reconstruction in ST40 and (b) Segmentation of the conductor wall

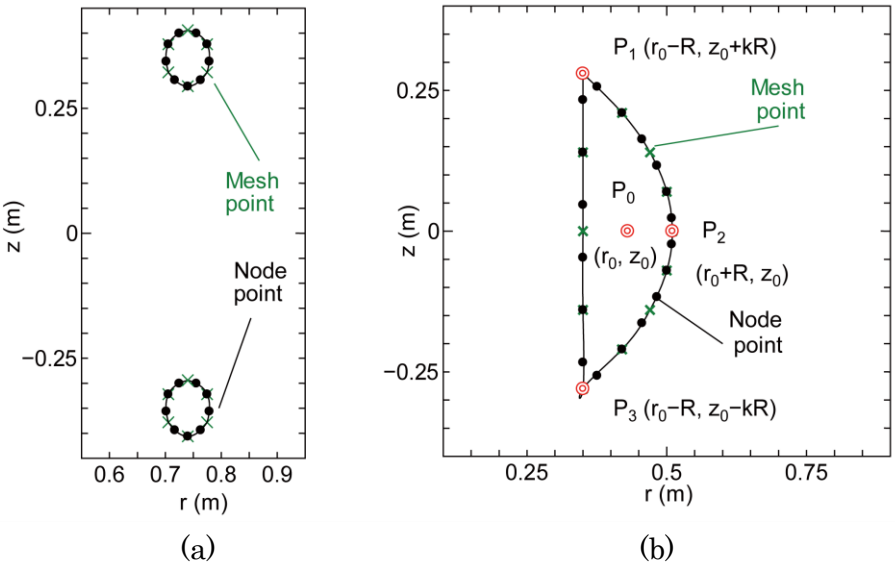

Fig. 7.13 The CCS segmentations at (a) 360 and 364 and (b) 368msec

phase	No. of CCSs	No. of boundary elements	No. of nodes
merging phase (360 and 364msec)	2	3×2	18
after merging (368msec)	1	6	18

Table. 7.3. The numbers of CCSs, boundary elements and nodes in each phase

7.5.3 Reconstructed poloidal flux profile and plasma boundary shape

The magnetic flux distributions were reconstructed in three representative time. Figures 7. 14 (a), (b) and (c) show the reconstructed flux profiles in each timing. In each figure the magenta dashed contours show the reference solution, while the black solid contours indicate the reconstructed solution (noise: 0 %). The blue, red, green solid lines show the reference plasma boundary, the reconstructed plasma boundary (noise: 0 %). As shown in Fig.14 in test calculation for ST40 reconstructed flux profile and plasma boundary agreed well with the reference profiles as well as in one for UTST even though the ST40 have in-vessel coil and complex conductor components. Similar to the test calculation for UTST, the error of the reconstructed boundary around X point was slightly large. However, the slightly large plasma boundary discrepancy around X point is also thought to be caused by the reference magnetic configuration itself and the reconstructed results of the test calculation in ST40 was also favorable for demonstrating this method in UTST experiment.

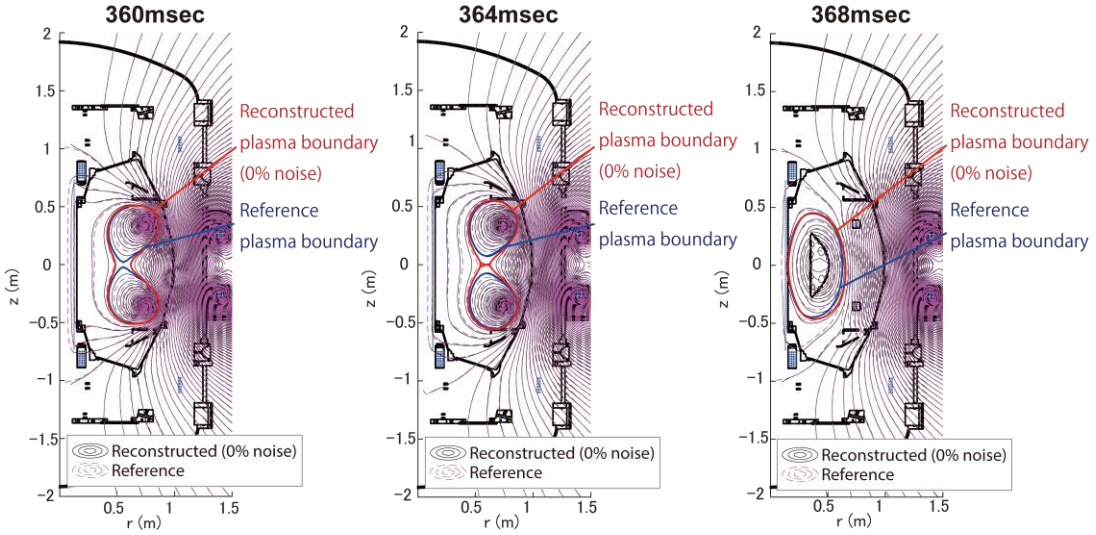

Fig. 7.14 The reconstructed poloidal flux profiles at 360, 364 and 368msec

7.6 Conclusion

The M-CCS method has been applied to reconstruct the plasma boundary shape as well as the eddy current profile for merging spherical tokamak in the UTST device. Achievement of this research are summarized below.

- Two CCSs were set on close to the each magnetic axis during merging to apply the M-CCS method merging operation.
- In UTST the plasma boundary shape has been reconstructed accurately using noiseless sensor signals, reconstructed with fairly good accuracy using sensor signals with 3 % noise. The eddy current profile has been also reconstructed with fairly good accuracy.
- In ST40 the plasma boundary shape has been reconstructed accurately using noiseless sensor signals as well as test calculation for UTST even though the ST40 have in-vessel coil and

complex conductor components.

From these test calculations preparation for experimental verification in UTST were complete. The author believe that this analytical technique is also useful for other axial plasma merging experiments. For example, in the doublet-shaped tokamak such as the doublet III (General Atomics) [55] and the TCV (SPC) [56, 57], merging of two droplet-shaped plasma is regarded as the preferred scenario for forming the configuration. The present technique can be also expected as an effective analytical tool for such a doublet-shaped configuration.

Chapter8

Conclusion

To investigate electron energization mechanism during ST merging start-up soft X-ray emission was observed by SBD and soft X-ray imaging system in UTST merging experiments. Experimental results are summarized below.

- Soft X-ray burst over 200eV was observed only during merging and the peak soft X-ray intensity showed positive dependency on the effective electric field around X point. The electron energy over 200eV was consistent with the result of simple 0D model calculation based on electron's duration of stay inside the reconnection region.
- 2D soft X-ray profile during merging was observed by soft X-ray imaging system. In very early phase of the merging relatively wide soft X-ray emission was observed in the downstream region and the emission finally formed the left-right asymmetric structure along a pair of the separatrix.
- In test particle calculation of electron acceleration, the soft X-ray emisson profile was accountable by the parallel acclereration by the induced toroidal electric field. This result suggests that in early phase of the merging when charge separation did not grow enough parallel electric field was induced not only inside diffusion region but also in the downstream region and the electrons in the downstream region were remarkably accelerated by the parallel electric field

These results give the following achievements.

- The electrons near the X point or downstream region are effectively accelerated in toroidal direction by the parallel electric field during plasma merging.
- The spatial profile of the accelerated electrons change with time phase during merging. In early phase when the charge separation do not still grow enough, accelerated electrons spread relatively wide area in the downstream region. Finally, in the almost steady phase of the reconnection the emission profile become the left-right asymmetric structures along a pair of the separatrix.

These results will be important knowledges for optimizing reconnection heating during ST merging. Especially it should be noted that in the early phase before charge separation grows, electrons are effectively energized in wide area of the downstream region. If such a condition can be maintained for a long period, effective electron heating may be realized during ST merging. However, in order to explore that potential, the detailed control of the merging process including merging speed must be required.

Furthermore, to investigate how the accelerated electrons affect the final ST equilibrium after merging, particularly the electron temperature, plasma shape reconstruction technique of merging plasma was developed. The M-CCS method has been applied to reconstruct the plasma boundary shape as well as the eddy current profile for merging ST in the UTST and ST40. Achievements of this research are summarized below.

- Two CCSs set near the each magnetic axis during merging to provide accurate reconstruction of the plasma shape by the M-CCS method.

- In UTST the plasma boundary shape has been reconstructed accurately using noiseless sensor signals, reconstructed with fairly good accuracy using sensor signals with 3 % noise. The eddy current profile has been also reconstructed with fairly good accuracy.
- In ST40 the plasma boundary shape has been reconstructed accurately using noiseless sensor signals as well as test calculation for UTST even though the ST40 have in-vessel coils and complex conductor components.

From these test calculations preparation for experimental verification in UTST was completed. The author believe that this analytical technique is also useful for the detailed control of the merging plasma.

Acknowledgement

本研究を遂行するにあたり多くの方々にご協力いただいた事を感謝申し上げます。指導教官である井先生には入学当初からとにかくお世話になりました。自慢ではありませんが今まで井先生が指導してきた博士学生の中で私は恐らくあらゆる面で最もレベルが低い学生であったと自覚しております。なかなか話がわからない上，伝わらない学生でありどう指導すればいいのかかなり苦労されただろうと思います。そんな私を入学当初から５年にわたり懲りずに丁寧に指導していただいただいたことを本当に感謝しております。井先生は研究において非常に寛容で，日ごろから学生に簡単に答えを与えずに遠回りしてでも自らの力で考えさせることで，自分の力で答えにたどり着く喜びや，をやり遂げる事の達成感を与えてくれる，そんな先生だったように思います。僕も井先生に導かれていることを脳裏で薄々気づきながら，意識の中では自由にいろいろなことに取り組み，多くの失敗をしながら自らの力で研究を進め，時には何らかの成果を手に入れ，時には無駄骨に終わるという経験を繰り返してくるうちにダメながらも少しずつでも成長をしてこれた気がしています。その中で時間の制約や，自らの力不足から安易に答えを手に入れてしまった研究におけるいくつかのことについては今でももったいなく思っています。また，井先生がいつかの複雑理工学専攻の送別会でおっしゃっていた，計画に沿って何かを実現する際には失敗することを前提に計画を立てることが大事だという話が自分の心の中には残っています。私はこの考え方が非常に好きで，そのことを念頭に研究を進めてくることでなんとかここまでやってこれたと感じています。気分屋であったことも非常に迷惑をかけました。何かを意欲的にやり始めたと思ったら次の瞬間に沈んでやる気を失ったり，理解に苦しむようなアップダウンも多くあったかもしれません。博士１年に上がるころ自ら提案した SBD による多チャンネル計測も，博士２年になって再度提案されて「僕はもうそれをやる気はないです。」と突っぱねたりもしました。博士２年になり UTST 装置に所属する学生の最上級生になってからについては特に自分の力不足を痛切に感じており，自分なりにやり切ったという気持ちもありますが，もう少し自分に何かできなかっただろうかと思うことも多くあります。数多くのご迷惑をおかけしてきましたが，先生のおかげで入学当初の自分のひどさを思い返せば少しはましになれたのではないかと思っております。那珂に行ってからは大学との接点はかなり少なくなってしまうと思いますが，どこかの学会でお会いできることを楽しみにしています。UTST 装置がこれから装置として多くの成長を遂げて，球状トカマク合体の実現のために新たな可能性を拓き，多くの研究成果をあげることを祈っております。そのために僕に貢献できることがあれば今後もこの業界にいれる限りは非力ながらできる限りの

協力をさせていただきたいと思います。

また，研究室の教授である小野靖先生には研究室内のミーティングや出張先の学会，また博士論文審査で非常に有益な意見・助言をいただきました。産総研の小口治久先生には軟X線計測の立ち上げの際に計測系の提供や多くの相談に乗っていただきました。それをスタートに一つずつ研究を積み上げてくることができました。感謝申し上げます。また，京都工芸繊維大学の三瓶明希夫先生には AXUV アレイ，軟X線イメージングシステムの設計，計測において多くの助言をいただきました。何度かこちらから京都工繊にお邪魔させていただいたり，遠方から柏に来ていただいて実験に協力していただいたりしたおかげで何とかかたちになる結果を得ることができたと考えています。AXUV については博士課程初期にかなり力を入れて立ち上げた計測系として思い入れがあり，博士論文の一部としてかたちにすることができなかった事が本当に悔やまれます。研究の手を広げすぎてしまったことで，他の研究と並行して進めることができず，博士課程中盤から思うような進展を得ることができなかった事，最後まで自分一人でやり抜く力がなかった自分の不甲斐なさを感じます。

北海道大学の板垣正文先生には CCS 法のコードの中でも最先端の修正 CCS 法のコード提供をいただきました。東大に入る以前学部時代に研究室に所属していた縁もあり，贔屓していただき懇切丁寧に手法やコードの中身の解説をしていただきました。また，論文の指導の他，研究者としての心構え，仕事のやり方など，豊かな経歴と経験から多くの事を教わりました。未だ実践できていないことばかりですが頭の中に多くの言葉が残っています。残された時間で必ずや UTST における CCS 実装を実現，少なくともそれに近いところへもっていきたいと思います。また，CCS 研究にかかわった一人の研究者として板垣先生の CCS に関する研究成果，また境界要素法に基づくプラズマ内部電流再構成の成果が世界中の多くの研究者に正しく認知され幅広く役に立つことを願っています。九州大学の中村一男先生には主に VEST 装置における修正 CCS 法の応用についていろいろ有益な意見をいただきました。なかなか博士課程の後半に一つの研究に集中して時間を割くことができず，その後に成果をあまり伝えることができなかったのが非常に残念です。多くの有益な意見は UTST への実装にも必ず役に立つものになるはずです。トカマクエナジーの Steven McNamara からは ST40 への CCS 法の応用のためのテスト計算用の正解の提供をいただきました。ST40 を一度は見てみたいと思っていましたが行けずに残念です。ST40 の計画が成功することを祈っています。ソウル国立大学の Yong-Seok Hwang 先生，Jeong-hun Yan 君には今回の博士論文には入りませんでしたが VEST での CCS 法応用のための磁気データの提供をいただきました。Hwang 先生は A3 でお会いする際にもソウル国立大学にうかがわせていただいた際にもホスピタリティがすごく，非常に良くしていただいた印象があります。その他ソウル大学の学生にもソウルに行った際にはいろいろ案内してくれたりおいしいものを食べさせていただいたりとても楽しい思い出があります。英語がもっとうまく喋れればもっと仲良くなれた気がします。将来どこかの学会で会えることを密かに願っています。

また，台湾成功大学の河森栄一郎先生には共同研究で柏にいらした際や学会でお会いした際に，いつも気にかけて研究の進展状況について聞いていただいて，厳しいながらも核心をついた第三者からの立場の的確な意見を多くいただきました。感謝申し上げます。また，研究室の OB である九州大学の山田琢磨先生は一か月しか研究室にいた時期はかぶっていませんがその後も計測データ取り込みシステムや，解析システムについて度々教えていただいてお世話になりました。毎回柏に来るたびに飲み会に誘っていただいたこともいい息抜きになり楽しかったです。

また，お会いしたことがない方も数多くおりますが，UTST 装置の立ち上げ，創世記に携わり今日にまでに利用され続けている実験・計測システムを開発してくれた諸先輩方をはじめ，直接お世話になった先輩方，同期，後輩方のサポートにより自らの研究をここまで遂行できたことを感謝申し上げます。

最後に，合体立ち上げの研究に少しでも携わった者として，将来球状トカマク合体による立ち上げが実現するしないにかかわらず，球状トカマク合体立ち上げの可能性が今後研究され尽くされその他多くの分野の研究に役立つことを願っています。

References

[1] Y. -K. M. Peng, Phys. Plasmas 7, 1681-1692 (2000)

[2] J. G. Cordey, C. D. Challis, and P. M. Stubberfield, Plasma Phys. Control. Fusion 30, 1625 (1988)

[3] R. D. Stambaugh, V. S. Chan, R.L. Miller, and M.J. Schaffer, Fusion technology 33, 1 (1998)

[4] M. Ono, and R. Kaita, Physics of Plasmas 22, 040501 (2015)

[5] Y. Takase, T. Fukuda, X. Gao, M. Gryaznevich, S. Itoh, Y. Kamada, et al., Plasma Fusion Res 78, 719-721 (2002)

[6] R. L. Miller, Y. R. Lin-Liu, A. D. Turnbull, V. S. Chan, L. D. Pearlstein, O. Sauter, et al., General Atomics Report, GA-A22433

[7] J. E. Menard, S. C. Jardin, S. M. Kaye, C. E. Kessel, and J. Manickam, Nucl. Fusion 37, 595 (1997)

[8] V. F. Shevchenko, M. R. O'Brien, D. Taylor, A. N. Saveliev, and MAST team, Nucl. Fusion 50, 022004 (2010)

[9] M. Uchida, T. Yoshinaga, H. Tanaka, and T. Maekawa, Phys. Rev. Lett 104, 065001 (2010)

[10] T. Shinya, Y. Takase, S. Yajima, C. Moeller, H. Yamazaki, N. Tsujii, et al., Nucl. Fusion 57, 036006 (2016)

[11] R. Raman, B. A. Nelson, M. G. Bell, T. R. Jarboe, D. Mueller, T. Bigelow, et al., Phys. Rev. Lett 97, 175002 (2006)

[12] M. Nagata, T. Kanki, N. Fukumoto, and T. Uyama, Physics of Plasmas 10, 2932-2939 (2003)

[13] A. J. Redd, T. R. Jarboe, W. T. Hamp, B. A. Nelson, R. G. O'Neill, and R. J. Smith, Physics of Plasmas 15, 022506 (2008)

[14] D. J. Battaglia, M. W. Bongard, R. J. Fonck, A. J. Redd, and A. C. Sontag, Phys. Rev. Lett 102, 225003 (2009)

[15] O. Mitarai, Plasma Phys. Control. Fusion 41, 1469–1483 (1999)

[16] S. Shiraiwa, S. Ide, S.Itoh, O. Mitarai, O. Naito, T. Ozeki, et al., Phys. Rev. Lett 92, 035001 (2003)

[17] J. Kim, W. Choe, and M. Ono, Plasma Phys. Control. Fusion 46, 1647–1657 (2004)

[18] Y. Ono, T. Kimura, E. Kawamori, Y. Murata, S. Miyazaki, Y. Ueda, et al., Nucl. Fusion 43, 789-794 (2003)

[19] M. Inomoto, T.G. Watanabe, K. Gi, K. Yamasaki, S. Kamio, R. Imazawa, et al., Nucl. Fusion

95, 033013 (2015)
[20] I. T. Chapman, J. Adamek, R. J. Akers, S. Allan, L. Appel, O. Asunta, et al., Nucl. Fusion 55 (2015) 104008
[21] H. Tanabe, T. Yamada, T. Watanabe, K. Gi, M. Inomoto, R. Imazawa, et al., Nucl. Fusion 57 (2017) 056037
[22] M. Gryaznevich, V. Shevchenko and A. Sykes, Nucl. Fusion 46 (2006) S573
[23] M.P. Gryaznevich and A. Sykes, Nucl. Fusion 57 (2017) 072003
[24] P.F. Buxton, M.P. Gryaznevich and Tokamak Energy Ltd. team, Fusion Eng. Des 123 (2017) 551-554
[25] R. Imazawa, S. Kamio, R. Hihara, K. Abe, M. Sakumura, Q. Cao, et al., Electrical Engineering in Japan 179 (2012) 18-24
[26] T. Yamada, R. Imazawa, K. Kamio, R, Hihara, K. Abe, M. Sakumura, et al., Plasma Fusion Res 5 (2010) S2100
[27] M. Gryaznevich, O. Asunta and Tokamak Energy Ltd. team, Fusion Eng. Des 123 (2017) 177-180
[28] M. Gryaznevich, 電気学会論文誌 A, Vol.125, No.11, p.881-886 (2005)
[29] Y. Ono, H, Tanabe, Y. Hayashi, T. Ii, Y. Narushima, T. Yamada, et al., Phys. Rev. Lett. 107 (2011) 185001
[30] E. N. Parker, J. Geophys. Res. 62 (1957) 509
[31] Drake, J., and M. Shay, 2007, in Reconnection of Magnetic Fields: Magnetohydrodynamics and Collisionless Theory and Observations, edited by J. Birn and E. R. Priest (Cambridge University Press, Cambridge), p. 87
[32] Y. Ono, M. Inomoto, T. Okazaki and Y. Ueda, Phys. Plasmas 4 (1997) 1953
[33] J.D. Huba, Phys. Plasmas 12 (2005) 012322
[34] Y. Ono, H. Tanabe1, T. Yamada, M. Inomoto, T. Ii, S. Inoue, et al., Plasma Phys. Control. Fusion 54 (2012) 124039
[35] P. L. Pritchett, Physics of Plasmas 12 (2005) 062301
[36] T. Yamada, H. Tanabe, T.G. Watanabe, Y. Hayashi, R. Imazawa, M. Inomoto, et al., Nucl. Fusion 56 (2016) 106019
[37] P. K. Browning, S. Cardnell, M. Evans, F. Arese Lucini, V. S. Lukin, K. G. McClements, et al., Plasma Phys. Control. Fusion 58 (2016) 014041
[38] NIST website (http://www.nist.gov/pml/data/asd.cfm)
[39] M. Galanti, R. Gott and J.F. Renaud, Rev. Sci. Inst 42 (1971) 1818
[40] T. Ushiki, M. Inomoto, K. Yamasaki, X. Guo, T. Sugawara, K. Matsuyama, et al., Plasma Fusion Res. 11 (2016) 2402100
[41] X. Guo, M. Inomoto, T. Sugawara, K. Yamasaki, T. Ushiki, Y. Ono, et al., Phys. Plasmas

22 (2015) 101201
[42] B. Lloyd, G.L. Jackson, T.S. Taylor, E.A. Lazarus, T.C. Luce and R. Prater Nucl. Fusion 31 (1991) 2031
[43] K. Kurihara, Fusion Eng. Des 51-52 (2000) 1049-1057
[44] Y. Miyata, S. H. Hahn, T. Suzuki, S. Ide, J. Chung, J. G. Bak, et al., Physics of Plasmas 21 (2016) 032502
[45] Y. Miyata, T. Suzuki, M. Takechi, H. Urano, and S. Ide, Rev. Sci. Instrum. 86 (2016) 073511
[46] K. Nakamura, Y. Jiang, X. L. Liu, O. Mitarai, K. Kurihara, Y. Kawamata, et al., Fusion Eng. Des 86 (2011) 1080–1084
[47] M. Itagaki, T. Maeda, T. Ishimaru, G. Okubo, K. Watanabe, R. Seki, et al., Plasma Phys. Control. Fusion 53 (2011) 105007
[48] M. Itagaki, G. Okubo, M. Akazawa, Y. Matsumoto, K. Watanabe, R. Seki, and Y. Suzuki, Plasma Phys. Control. Fusion 54 (2012) 125003
[49] M. Itagaki, K. Ishimaru, Y. Matsumoto, K. Watanabe, R. Seki, and Y. Suzuki, Plasma Fusion Res 8 (2013) 1402134
[50] M. Itagaki, A. Sanpei, S. Masamune, and K. Watanabe, Plasma Fusion Res 9 (2014) 1402046
[51] L.L. Lao, H. St. John, R.D. Stambaugh, A.G. Kellman and W. Pfeiffer, Nucl. Fusion 25 (1985) 1611
[52] M. Itagaki, J. Kamisawada, S. Oikawa, Nucl. Fusion 44 (2004) 427-437
[53] P. C. Hansen, Rank-Deficient and Discrete Ill-Posed Problems – Numerical Aspects of Linear Inversion (Philadelphia, SIAM, 1998).
[54] P.C. Hansen, Rank-Deficient and Discrete Ill-Posed Problems – Numerical Aspects of Linear Inversion (Philadelphia: SIAM, 1998).
[55] J. C. Wesley, T. Angel, C. J. Armentrout, D. R. Baker, F. P. Blau, G. Bramson, et al., in Plasma Physics and Controlled Nuclear Fusion Research (Proc. 8th Int. Conf. Brussels, 1980) Vol. 1, IAEA, Vienna (1981) 35
[56] F. Piras, EPFL Thesis 5015 (2011)
[57] J. Sinha, EPFL Thesis 7825 (2017)

Research achievements

1. 学術論文（査読有）

1) T. Ushiki, M. Inomoto, M. Itagaki, “Reconstruction of Plasma Shape and Eddy Current Profile based on Modified Cauchy Condition Surface Method in Merging Spherical Tokamak” , Fusion Eng. Des 122, 35-41 (2017)

2) T. Ushiki, M. Inomoto, K. Yamasaki, X. Guo, T. Sugawara, K. Matsuyama, H. Koguchi, T. Yamada, ”Generation of Energetic Electrons during Spherical Tokamak Merging in UTST”, Plasma Fusion Res. 11, 2402100 (2016).

3) K. Yamasaki, , S. Inoue, S. Kamio, T. G. Watanabe, T. Ushiki, X. Guo, T. Sugawara, K. Matsuyama, N. Kawakami, T. Yamada, M. Inomoto, Y. Ono, “Laboratory study of diffusion region with electron energization during high guide field reconnection”, Phys. Plasmas 22, 101202 (2015).

4) X. Guo, M. Inomoto, T. Sugawara, K. Yamasaki, T. Ushiki, Y. Ono, TS Group, “Localized electron heating by strong guide-field magnetic reconnection”, Phys. Plasmas 22, 101201 (2015).

5) M. Inomoto, T.G. Watanabe, K. Gi, K. Yamasaki, S. Kamio, R. Imazawa, T. Yamada, X. Guo, T. Ushiki, H. Ishikawa, H. Nakamata, N. Kawakami, T. Sugawara, K. Matsuyama, K. Noma, A. Kuwahata, H. Tanabe, ”Centre-solenoid-free merging start-up of spherical tokamak plasmas in UTST”, Nucl. Fusion 55, 033013 (2015).

6) X. Guo, M. Inomoto, T. Sugawara, T.G. Watanabe, K. Yamasaki, T. Ushiki, Y. Ono, “Two-Dimensional Electron Temperature and Density Measurement during Strong Guide-Field Reconnection by using Slide-Type Thomson Scattering System” , Plasma Fusion Res. 10, 3402017 (2015).

7) 牛木知彦, 井通暁, 小口治久, 「球状トカマク合体時の磁気リコネクションにおける軟X線放射の観測」, 電気学会論文誌A, Vol.134, No.9, p.493-496 (2014).

2. 国際会議（口頭発表，査読なし）

1) T. Ushiki, M. Itagaki, M. Inomoto, “Plasma shape reconstruction of merging spherical tokamak in UTST device”, 5th A3 Foresight Workshop on Spherical Torus, Kunming, China, February 15-17, 2017

2) M. Inomoto, K. Yamasaki, T. Ushiki, X. Guo, T. Sugawara, K. Matsuyama, N. Kawakami, A. Sato, Y. Fukai, H. Yamanaka, R. Tamura, H. Tanabe, Y. Ono, “Particle acceleration in magnetic reconnection laboratory experiment with presence of strong guide field”, 18th International Congress on Plasma Physics, Kaohsiung, Taiwan, June 27-July 1, 2016

3) M. Inomoto, K. Yamasaki, T. Ushiki, X. Guo, N. Kawakami, T. Sugawara, K. Matsuyama, A. Sato, K. Noma, Y. Fukai, H. Yamanaka, R. Tamura, A. Kuwahata, H. Tanabe, Y. Ono, T. I. Tsujimura, S. Kamio, T. Yamada, “Center-Solenoid-Free Merging Start-up of STs by Outer PF coils in UTST”, 18th International Spherical Torus Workshop, Princeton, USA, November 3-6, 2015

4) M. Inomoto, K. Yamasaki, T. Ushiki, X. Guo, N. Kawakami, T. Sugawara, K. Matsuyama, A. Sato, K. Noma, Y. Fukai, H. Yamanaka, R. Tamura, A. Kuwahata, H. Tanabe, Y. Ono, “Merging formation of high-beta ST as a target plasma for NBI”, 2015 US-Japan Compact Torus Workshop, Tokyo, September 11, 2015

5) T. Ushiki, H. Furui, K. Matsuyama, H. Koguchi, M. Inomoto, Y.Ono, “Study of Electron Acceleration during Spherical Tokamak Merging in UTST device”, 3rd A3 Foresight Workshop on Spherical Torus, Kisarazu, Japan, December 15-17, 2014

6) M. Inomoto, T.G. Watanabe, K. Yamasaki, A. Wang, T. Ushiki, X. Guo, H. Ishikawa, H. Nakamata, N. Kawakami, T. Sugawara, K. Matsuyama, Y. Ono, “Merging startup of high beta spherical tokamak by using outer poloidal field coils", Workshop on Exploratory Topics in Plasma and Fusion Research (EPR) and US-Japan Compact Torus (CT) Workshop, August 5-8, 2014

7) M. Inomoto, T.G. Watanabe, K. Yamasaki, A. Wang, T. Ushiki, X. Guo, H. Ishikawa, H. Nakamata, A. Kuwahata, R. Yanai, Y. Ono, “Observation of Energetic Electrons Generated

during Guide Field Reconnection", US-Japan Workshop on Magnetic Reconnection MR2014, May 20-24, 2014

3. 国際会議（ポスター発表，査読あり）

1) M. Inomoto, K. Yamasaki, T. Ushiki, X. Guo, S. Kamio, R. Yanai, T. Sugawara, Y. Fukai, H. Yamanaka, R. Tamura, "Formation of Closed Flux Surfaces in Reconnection Current Layer by Accelerated Electrons during Merging Start-up of Spherical Tokamak", 26th IAEA Fusion Energy Conference, Kyoto, Japan, Oct. 17-22, 2016

2) M. Inomoto, T.G. Watanabe, K. Yamasaki, S. Kamio, T. Yamada, A. Wang, X. Guo, T. Ushiki, H. Ishikawa, H. Nakamata, H. Itagaki, A. Kuwahata, B. Gao, R. Yanai, "Generation of Energetic Electrons by Magnetic Reconnection with Presence of High Guide Field", 25th IAEA Fusion Energy Conference, Saint Petersburg, Russia, Oct. 13-18, 2014

4. 国際会議（ポスター発表，査読なし）

1) T. Ushiki, T. Mihara, M. Inomoto, T. Sugawara, K. Kondo, Y. Minami, Y. Inai, H, Tanabe, Y. Ono, H. Koguchi, A. Sanpei, "Observation of energetic electrons using 2D soft X-ray measurements during spherical tokamak merging in UTST device", Plasma Conference 2017, Himeji, Japan, November 20-24, 2017

2) T. Ushiki, M. Inomoto, M. Itagaki, S. McNamara, "Plasma shape reconstruction for merging spherical tokamak based on modified CCS method", 58th Annual Meeting of the APS Division of Plasma Physics, Milwaukee, Wisconsin, USA, October 23-27, 2017

3) T. Ushiki, M. Inomoto, M. Itagaki, S. McNamara, "Plasma shape reconstruction of merging spherical tokamak", 19th International Spherical Torus Workshop, Seoul, Korea, September 19-22, 2017

4) T. Ushiki, M. Itagaki, M. Inomoto, "Shape reconstruction of merging spherical tokamak plasma in UTST device", 58th Annual Meeting of the APS Division of Plasma Physics, San Jose, California, USA, October 31-November 4, 2016

5) T. Ushiki, M. Itagaki, M.Inomoto, "Shape reconstruction of merging spherical tokamak plasma

in UTST device", JSPS A3 Foresight Program 4th Summer School on Spherical Torus, Hakata, Japan, August 2-5, 2016

6) T. Ushiki, M. Itagaki, M. Inomoto, "Shape reconstruction of merging spherical tokamak plasma using only external magnetic sensor signal in UTST device", 18th International Congress on Plasma Physics, Kaohsiung, Taiwan, June 27-July 1, 2016

7) T. Ushiki, H. Furui, K. Matsuyama, H. Koguchi, M. Inomoto, "Generation of Energetic Electrons during Spherical Tokamak Merging in UTST", 25th International Toki Conference, Gifu, Japan, November 3-6, 2015

8) T. Ushiki, H. Furui, K. Matsuyama, H. Koguchi, M. Inomoto, "Generation of energetic electrons during spherical tokamak merging in UTST device", JSPS A3 Foresight Program 3rd Summer School on Spherical Torus, Chengdu, China, July 27-29, 2015

9) M. Inomoto, T.G. Watanabe, K. Yamasaki, T. Ushiki, X. Guo, H. Ishikawa, H. Nakamata, Y. Ono, "High-beta spherical tokamak start-up by using outer PF coils and plasma merging in UTST", Plasma Conference 2014, Niigata, Japan, November 18-21, 2014

10) T. Ushiki, K. Ishiguchi, K. Matsuyama, H. Koguchi, M. Inomoto, "Study of Electron Acceleration during Magnetic Reconnection in UTST device", Plasma Conference 2014, Niigata, Japan, November 18-21, 2014

11) T. Ushiki, T.G. Watanabe, K. Yamasaki, A. Wang, H. Ishikawa, X. Guo, H. Nakamata, H. Koguchi, M. Inomoto, Y. Ono, "Observation of Soft X-ray Emission during Spherical Tokamak Merging in UTST", JSPS A3 Foresight Program 2nd Summer School on Spherical Torus, Jeju, Korea, June 30-July 4, 2014

5. 国内学会・研究会における発表（査読なし）

1) 三原卓己，牛木知彦，井通暁，「UTST 球状トカマク合体実験における軟 X 線トモグラフィーシステムの開発」，平成 29 年電気学会全国大会，富山大学, 2016 年 3 月

2) 牛木知彦, 板垣正文, 井通暁, 「UTST 合体プラズマにおける CCS 法を用いたプラズマ位置形状および渦電流分布再構成」，第 33 回プラズマ・核融合学会年会，東北大学, 2016 年 11 月 29－12 月 1 日

3) 牛木知彦, 板垣正文, 井通暁, 「UTST 合体プラズマにおける外部磁気センサーのみでのプラズマ位置形状同定可能性の検討」, ST 研究会, 核融合研, 2016 年 9 月

4) 牛木知彦, 板垣正文, 井通暁, 「UTST 合体プラズマにおける CCS 法を用いたプラズマ位置形状および渦電流分布再構成」, 第 11 回核融合エネルギー連合講演会, 九州大学伊都キャンパス, 2016 年 7 月

5) 井通暁, 牛木知彦, 郭学瀚, 山田琢磨, 神尾修治, 山崎広太郎, 菅原拓路, 深井優介, 山中晴揮, 田村峻, 田辺博士, 小野靖, 「プラズマ合体を用いた球状トカマクの立ち上げと加熱」, 第 11 回核融合エネルギー連合講演会, 九州大学伊都キャンパス, 2016 年 7 月

6) 牛木知彦, 郭学瀚, 古井宏和, 松山敬太, 小口治久, 井通暁, 「UTST 装置における球状トカマク合体立ち上げ時の高エネルギー電子生成について」, ST 研究会, 核融合研, 2015 年 8 月

7) 牛木知彦, 古井宏和, 松山敬太, 小口治久, 「球状トカマク合体時における磁気リコネクション由来の高速電子の検証」, CTRFP 研究会, 核融合研, 2014 年 12 月

8) 牛木知彦, 石口孝治, 松山敬太, 小口治久, 井通暁, 「UTST 装置における磁気リコネクション由来の高速電子の検証」, ST 研究会, 核融合研, 2014 年 8 月

9) 牛木知彦, 渡辺岳典, 山崎広太郎, 王安斉, 石川裕貴, 郭学瀚, 中俣浩樹, 小口治久, 井通暁, 小野靖, 「UTST 球状トカマク合体実験における磁気リコネクション時の軟 X 線放射の観測」, 第 10 回核融合エネルギー連合講演会, 筑波, 2014 年 6 月

6. 受賞歴

- Poster award of JSPS A3 Foresight Program 3rd Summer School on Spherical Torus 2015 (T. Ushiki, H. Furui, K. Matsuyama, H. Koguchi, M. Inomoto, “Generation of energetic electrons during spherical tokamak merging in UTST device”, JSPS A3 Foresight Program 3rd Summer School on Spherical Torus, Chengdu, China, July 27-29, 2015)